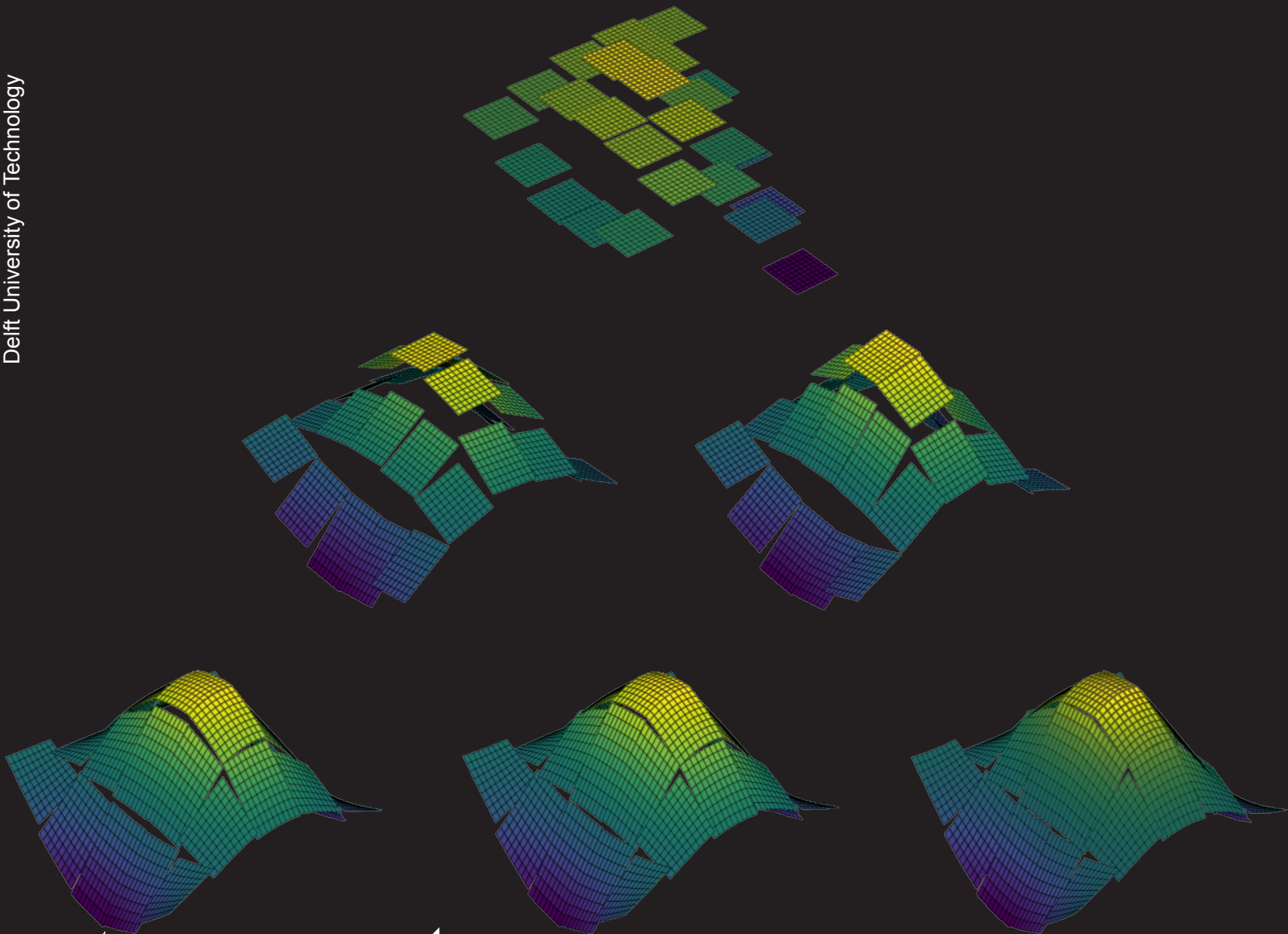


# Reconstructed discontinuous Galerkin methods for high Reynolds number flows

Master Thesis  
Malte Wegener

Delft University of Technology





# Reconstructed discontinuous Galerkin methods for high Reynolds number flows

Master Thesis

by

Malte Wegener

to obtain the degree of Master of Science at the Delft University of Technology,  
to be defended publicly on 8<sup>th</sup> of December 2022.

Student number:	4672194	
Thesis Committee:	Dr. M. Gerritsma	TU Delft
	Dr. S. J. Hulshoff	TU Delft
	Dr. B. Giovanardi	TU Delft
	T. Leicht	DLR Braunschweig

An electronic version of this thesis is available at <http://repository.tudelft.nl/>.



# Abstract

Reconstructed Discontinuous Galerkin (rDG) methods aim to provide a unified framework between Discontinuous Galerkin (DG) and finite volume (FV) methods. This unification leads to a new family of spatial discretization schemes from order three upwards. The first of these new schemes is the rDG(P1P2) method, which represents the solution on each element as linear functions while reconstructing quadratic contributions to compute the fluxes inside the element and over the faces. For the rDG(P1P2) method, two different reconstruction methods were implemented. The first of these reconstruction methods is a least-squares based reconstruction. For this reconstruction, an inverse distance weighting was introduced to improve the discretization error in anisotropic mesh regions, as well as an extended reconstruction stencil variant, which aims to stabilise the reconstruction on simplicial meshes. The inclusion of an inverse distance weighting was found to be beneficial for high Reynolds number flows on the example of the two-dimensional zero pressure gradient flat plate. As a second method, a variational reconstruction method was implemented. For the variational reconstruction rDG methods it was shown that they can offer significantly reduced discretization errors compared to DG methods for smooth flows. It was shown on the example of a method of manufactured solutions, that all implemented methods reach their designed order of accuracy and can provide lower spatial discretization errors than a DG method of a comparable order on regular and randomly perturbed hexahedral meshes as well as on tetrahedral meshes. The rDG methods was applied to several two and three-dimensional RANS test cases. For these test cases, a stronger influence of the Reynolds number on the discretization error of rDG methods was found compared to the weaker influence observed for DG methods. For all test-cases, it was shown that rDG methods converge faster on the same mesh, however, yield a higher absolute error, due to the lower number of degrees of freedom compared to native DG methods.



# Preface

This thesis concludes my five years at TU Delft, even though I have only spent three of these years actually in Delft. Even though the workload was quite challenging at times, I thoroughly enjoyed my time at Delft and believe it prepared me very well for my future life.

I would like to thank both my supervisors, Tobias and Steve, for their valuable input during the entire research project. I especially appreciated, that you gave me the opportunity to make this project my own, by letting me follow my own ideas. I appreciated the input you gave me during this project which brought this thesis to a very satisfying end for me.

I would also like to thank my friends both at home and in Braunschweig for being there during my thesis. Finally and most importantly I want to thank my parents, Christiane and Dieter, and my little sister, Fenja, for enabling me to study at Delft and supporting me during my whole studies. Thank you also for making me aware of Delft in the first place, without your engagement I would not be where I am now.

*Malte Wegener  
Braunschweig, November 2022*



# Contents

Abstract	iii
List of Figures	ix
List of Tables	xi
List of Symbols and Abbreviations	xiii
1 Introduction	1
2 Discontinuous Galerkin discretization of the RANS equations	3
2.1 Governing equations	3
2.1.1 Euler equations	3
2.1.2 Reynolds averaged Navier Stokes equations	3
2.2 Orthornormal basis DG formulation	4
2.3 Inviscid flux computation	5
2.4 Viscous flux computation	5
2.4.1 BR1 scheme	5
2.4.2 BR2 scheme	5
3 Reconstructed Discontinuous Galerkin	7
3.1 Preliminaries	7
3.2 Viscous flux computation in reconstructed DG methods	8
3.3 Reconstruction methods	10
3.3.1 Least-squares Reconstruction	10
3.3.2 Variational Reconstruction	11
3.4 State of the art	12
3.4.1 Least-squares Reconstruction	12
3.4.2 Variational Reconstruction	13
3.4.3 Research questions	13
4 Non-linear solution process	15
4.1 Discretization in pseudo time	15
4.1.1 Linearized implicit Euler	15
4.1.2 Switched evolution relaxation	15
4.2 Linear solution process	16
4.2.1 Preconditioned Krylov subspace methods	16
4.2.2 Usage of approximate Jacobians	16
5 Verification	17
5.1 Method of manufactured solution	17
5.2 Inviscid flows	18
5.2.1 Hexahedral meshes	18
5.2.2 Tetrahedral mesh	20
5.2.3 Extended stencil on isotropic meshes	20
5.2.4 Variational reconstruction on non-planar faces	21
5.3 Viscous flows	22
5.3.1 Hexahedral meshes	22
5.3.2 Tetrahedral mesh	23

5.4	Viscous treatment in rDG methods . . . . .	23
5.4.1	BR1 vs BR2 scheme . . . . .	24
5.4.2	Influence of the penalty parameter $\eta$ . . . . .	24
5.4.3	Stability of viscous fluxes. . . . .	25
5.4.4	Further treatment of viscous terms . . . . .	27
5.5	Conclusion . . . . .	27
6	Results . . . . .	29
6.1	General settings. . . . .	29
6.2	Smooth bump. . . . .	29
6.3	Zero pressure gradient flat plate. . . . .	31
6.4	Low Reynolds number airfoil . . . . .	33
6.5	High Reynolds number airfoil. . . . .	35
6.6	Multi Element airfoil . . . . .	36
6.7	Hemisphere-cylinder . . . . .	37
7	Conclusion . . . . .	41
7.1	Convergence of rDG methods. . . . .	41
7.2	Influence of the viscous flux in rDG methods . . . . .	41
7.3	Inverse distance weighting . . . . .	41
7.4	Applicability to high Reynolds number flows . . . . .	42
7.5	Jacobian approximation . . . . .	42
7.6	Influence of mesh quality . . . . .	42
7.7	Recommendations for future work . . . . .	42
	Bibliography . . . . .	43
A	Influence of the weighting on the condition number of reconstruction . . . . .	47

# List of Figures

3.1	"Classification of the proposed $P_N P_M$ schemes. The leftmost branch ( $N = 0$ ) coincides with standard finite volume schemes and the rightmost branch ( $N = M$ ) with classical DG schemes. From third-order on, there is a new class of intermediate schemes in between those branches." Figure adapted from [19] . . . . .	8
3.2	Comparison of the discretization for a sine wave between a DG(P1) (blue) and a rDG(P1P2) method (red). The exact sine wave is shown in black. . . . .	9
3.3	Number of Gauss quadrature points needed in 1 dimension for a selection of rDG methods . . .	9
3.4	(a) Compact face-based stencil on the example of a structured triangular mesh. (b) Extended node-based stencil on the example of a structured triangular mesh. From [43] . . . . .	11
5.1	Density Error against cube root of the number of degrees of freedom for the method of manufactured solution on a regular and randomly perturbed hexahedral mesh for the Euler equations.	19
5.2	Slice through the solution at $x = 0$ for (a) DG(P1) method, (b) a compact stencil least-squares rDG(P1P2) method and (c) a DG(P2) method. . . . .	19
5.3	Density Error against the number of degrees of freedom for the method of manufactured solution on an unstructured tetrahedral mesh for the Euler equations. . . . .	20
5.4	Density Error against cube root of the number of degrees of freedom on a regular hexahedral grid for three different stencil choices for a least-squares reconstruction on the example of the Euler equations. . . . .	21
5.5	Density Error against cube root of the number of degrees of freedom on a hexahedral mesh, a randomly perturbed hexahedral mesh and a parallelepiped mesh. . . . .	22
5.6	Density Error against cube root of the number of degrees of freedom on a regular hexahedral grid and a randomly perturbed hexahedral mesh for the RANS-SA-negative equations. . . . .	23
5.7	Density Error against cube root of the number of degrees of freedom on a tetrahedral mesh for the RANS-SA-negative equations. . . . .	24
5.8	Comparison of the density for the BR1 and BR2 scheme on a regular hexahedral grid for DG and rDG methods. . . . .	25
5.9	Influence of the $\eta$ parameter in the BR2 scheme on the Density Error on a hexahedral grid. . . .	26
5.10	(a) Comparison between the analytical and assumed first non-constant eigenmode. (b) Comparison between the 10 <sup>th</sup> analytical and assumed eigenmodes. (c) Comparison between the highest analytical and assumed eigenmodes . . . . .	27
5.11	(a) Approximate Eigenvalues and Numerical Stability Limits for rDG and DG Methods up to third order. (b) Approximate eigenvalues and numerical stability limits for rDG and DG methods up to second order. . . . .	28
6.1	(a) Finest mesh of the mesh cascade used for the smooth bump test case. (b) Mach Number distribution for the smooth bump test case. . . . .	30
6.2	Integrated entropy error of different rDG methods against the number of degrees of freedom for the smooth bump test case. . . . .	30
6.3	(a) Compact face-based stencil on the example of a structured quadrilateral mesh. (b) Extended node-based stencil on the example of a quadrilateral triangular mesh. . . . .	31
6.4	(a) Finest mesh in the mesh cascade for the flat plate test case from the NASA turbulence modelling resource. (b) Distribution of the transported turbulent variable close to the leading edge of the plate for the flat plate test case. . . . .	32
6.5	(a) Error of $C_D$ against the number of degrees of freedom per dimension for different discontinuous Galerkin and reconstructed discontinuous Galerkin methods. . . . .	32
6.6	Density error of rDG(P1P2) and DG(P1) methods against a DG(P2) solution for the flat plate test case on the finest mesh. . . . .	33

6.7	(a) Finest mesh of the mesh cascade used for the NACA0012 test case. (b) Mach number distribution of the converged third-order solution for the NACA0012 airfoil test case. . . . .	34
6.8	(a) Error of coefficient of drag against the number of degrees of freedom for the NACA0012 airfoil. (b) Error of coefficient of drag against computational time for the NACA0012 airfoil. . . . .	35
6.9	a) Finest mesh of the mesh cascade used for the Juskowski airfoil test case. (b) Mach number distribution of the converged third-order solution for the Juskowski airfoil test case. . . . .	35
6.10	(a) Coefficient of drag against the number of degrees of freedom for a Juskowski airfoil. (b) Coefficient of drag against computational time for a Juskowski airfoil. . . . .	36
6.11	(a) Medium mesh for the L1T2 airfoil consisting of quadratic hexahedrons. (b) DG(P2) solution of the flow around the L1T2 airfoil on the medium mesh. The jagged flow field contours do not arise from numerical artefacts, but from the projection of the solution onto the elements as an element average. . . . .	37
6.12	(a) Coefficient of drag in continuous lines and Coefficient of lift in dashed lines against the number of degrees of freedom for the L1T2 airfoil for different rDG and DG methods. (b) Coefficient of drag in continuous lines and Coefficient of lift in dashed lines against computational time for the L1T2 airfoil. . . . .	37
6.13	Finest hexahedral mesh for the Hemisphere-cylinder test case. . . . .	38
6.14	Coefficient of drag against the number of degrees of freedom for the Hemisphere-cylinder test case. . . . .	39
6.15	(a) Convergence of the density residual against the number of non-linear iterations for the Hemisphere-cylinder test-case. (b) Convergence of the density residual against total computational time for the Hemisphere-cylinder test case. . . . .	39
A.1	Condition numbers of the linear reconstruction problems against the normalized volume of the cell. . . . .	47

# List of Tables

4.1	Number of Block Jacobi preconditioning steps for each polynomial order of basis functions. . .	16
5.1	Parameters chosen for the manufactured solution . . . . .	18
5.2	Verification of the numerical methods for estimating the maximum eigenvalue of the discretization . . . . .	27
6.1	Drag Coefficients of the three finest grids for a DG(P2) method with the extrapolated value using the procedure by Celik et al. [12] . . . . .	31



# List of Symbols and Abbreviations

## Abbreviations

BE	Backwards Euler
CFD	Computational fluid dynamics
CFL	Courant-Friedrichs-Lewy
CODA	CFD for ONERA, DLR and Airbus
DG	Discontinuous Galerkin
DLR	German Aerospace Center
FV	Finite volume
GMRES	Generalized minimum residual method
NASA	National Aeronautics and Space Administration
ONERA	Office national études et de recherches aérospatiales
PDE	Partial differential equation
rDG	Reconstructed Discontinuous Galerkin
SER	Switched evolution relaxation

## Roman letters

$\bar{J}$	Linearized jacobian
$\bar{M}$	Mass matrix
$\mathbf{R}$	Residual
$\mathbf{u}$	State vector
$\mathbf{v}$	Velocity vector
$\mathcal{F}^c$	Convective flux
$\mathcal{F}^v$	Viscous flux
$\mathbb{P}^N$	Space of polynomials in $\mathbb{R}^3$ up to total order $N$
$F^c$	Convective numerical flux
$F^v$	Viscous numerical flux
E	Total energy

## Greek letters

$\mu_t$	Eddy viscosity
$\phi$	Basis function
$\rho$	Density
$\tilde{v}$	Spalart Allmaras transported variable



# 1

## Introduction

Current methods for computational fluid dynamics (CFD) for industrial applications are almost exclusively based on second-order finite volume schemes. These methods are very well-researched and have been applied to an extensive range of applications. With ever-increasing computational power, the possibility for methods of order higher than two increases significantly and there has been a significant effort in implementing these methods into industrial applications. The need for higher-order spatial discretization techniques has been laid out explicitly in the "CFD Vision 2030 Study" by NASA [44]. The usage of higher-order methods can be beneficial for scale-resolving simulations such as Large Eddy Simulations (LES), which are becoming ever more relevant in an industrial context. Even though there exist frameworks for constructing higher-order methods on unstructured grids, such as Galerkin spectral methods and higher-order finite volume schemes, their use for industrial applications remains limited. Due to the inherently higher coupling between the degrees of freedom in higher-order methods, the resulting numerical systems are significantly stiffer than lower-order methods and often less robust and harder to use.

Recently a novel method emerged as a hybrid version between second or higher-order finite volume methods and discontinuous Galerkin (DG) methods. The formulation is based directly on a DG method framework, however, during the solution process, higher-order moments of the solution are reconstructed similar to second and higher-order finite volume methods. The reconstructed discontinuous Galerkin (rDG) method aims to reduce the computational work needed for higher-order methods while keeping the advantageous properties of higher-order DG methods.

This thesis will evaluate the applicability of these rDG methods for high Reynolds number RANS simulations. For this, two different reconstruction techniques have been implemented. These are a least-squares reconstruction method and a more novel variational reconstruction method. For the least-squares reconstruction method, two extensions are proposed. The first extension employs an inverse-distance weighting to improve the reconstruction in highly anisotropic mesh regions such as boundary layers. Furthermore, an extended reconstruction stencil using a vertex-based neighbourhood is adapted from finite volume methods, to stabilise the method on simplicial meshes.

As variational reconstruction rDG methods have been found to be very hard to converge for complex flow problems in the context of a fully implicit solver. A simplification to the reconstruction process is proposed to allow convergence of the variational-reconstruction-based rDG method for high Reynolds number flows. The effect on accuracy of this simplification is examined.

The research objective is formulated as:

**Evaluate the applicability of higher-order compact reconstructed discontinuous Galerkin (rDG) discretizations for High Reynolds number RANS flows using least-squares reconstruction and variational reconstruction.**

The thesis will first introduce the modal DG formulation for the Euler and RANS equations in chapter 2. In chapter 3, the reconstructed DG method and the two reconstruction procedures used are introduced. At the end of this chapter, the research questions for this Thesis will be formulated. The non-linear solution process will be introduced in chapter 4.

In chapter 5, first, the implementation of the methods will be verified utilising the method of manufactured solutions. This tool will also be used to assess the influence of the diffusive flux treatment in rDG

methods compared to native DG methods. Chapter 6 will then compare rDG methods to native DG methods on the example of different test cases in two and three dimensions. Finally, chapter 7 will then summarise the results of chapters 5 and 6 and aims to answer the research questions established at the end of chapter 3.

The rDG methods of interest are integrated into the flow solver CODA. CODA is the computational fluid dynamics (CFD) software being developed as part of a collaboration between the French Aerospace Lab ONERA, the German Aerospace Center (DLR), Airbus, and their European research partners. CODA is jointly owned by ONERA, DLR and Airbus.

# 2

## Discontinuous Galerkin discretization of the RANS equations

The Discontinuous Galerkin (DG) method was first proposed by Reed and Hill [42] for the solution of the neutron transport equation. The method was later applied to the solution of the Euler equations [6], the compressible Navier-Stokes equations [5], and the Reynolds-averaged Navier-Stokes equations [10]. This chapter will first explain the governing Euler and Reynolds-averaged Navier-Stokes equations in section 2.1. In section 2.2, the DG formulation using orthonormal basis functions will be described. Sections 2.3 and 2.4 introduce the numerical fluxes used in the work.

### 2.1. Governing equations

This section will lay out the governing equations, and explicitly state the exact closures, which are used to close the system of equations in this study.

#### 2.1.1. Euler equations

The Euler equations describe the behaviour of a compressible fluid with no viscosity. They are a simplification of the Navier-Stokes equations and are purely hyperbolic. Due to the hyperbolic nature of the equations, they require no special treatment in DG discretizations and thus can be used to study the effect of the modifications in the discretization without the influence of viscous treatments laid out in section 2.4. The system of equations is shown in equation 2.1.

$$\nabla \cdot \mathcal{F}^C(\mathbf{u}) = \frac{\partial \mathbf{u}}{\partial t}, \quad (2.1)$$

where  $\mathcal{F}^C(\mathbf{u})$  is the vector of convective fluxes, with the vector of conservative variables

$$\mathbf{u} = \begin{bmatrix} \rho \\ \rho v_1 \\ \rho v_2 \\ \rho v_3 \\ \rho E \end{bmatrix}, \quad (2.2)$$

where  $\rho$  is the density of the fluid,  $v_i$  is the velocity of the fluid in the coordinate direction  $i$  and  $E$  is the specific total energy of the fluid. In this study, the ideal gas law is used to close the system of equations.

#### 2.1.2. Reynolds averaged Navier Stokes equations

The Reynolds averaged Navier Stokes (RANS) equations include the Euler equations, as well as diffusive fluxes, due to viscosity (eq. 2.3). The equations are furthermore Reynolds averaged, such that  $\mathbf{u} = \bar{\mathbf{u}} + \mathbf{u}'$ , where  $\bar{\mathbf{u}}$  is the steady state component, and  $\mathbf{u}'$  represents the fluctuating component of  $\mathbf{u}$ . The RANS equations are then formulated for the time-averaged component  $\bar{\mathbf{u}}$ , which will be represented by  $\mathbf{u}$  in the rest of this work, for simplicity's sake. The influence of  $\mathbf{u}'$  is modelled using an appropriate turbulence model

$$\nabla \cdot \mathcal{F}^C(\mathbf{u}) - \nabla \cdot \mathcal{F}^V(\mathbf{u}, \nabla \mathbf{u}) = \frac{\partial \mathbf{u}}{\partial t}, \quad (2.3)$$

The state vector and convective fluxes are unchanged from the Euler equations. However, an additional viscous flux term, is present. The diffusive flux  $\mathcal{F}^V(\mathbf{u}, \nabla \mathbf{u})$  depends on the viscosity of the fluid  $\mu$ . To calculate the spatially varying viscosity of the fluid, Sutherland's Law is used [47].

**Spalart-Allmaras turbulence model** The Spalart-Allmaras (SA) one-equation turbulence model was formulated by Spalart and Allmaras [45] and has since been widely used for external aerodynamic flows and in the latest Higher-Order workshops<sup>1</sup>. The model is used in its negative formulation for this study, which aims to address issues on under-resolved grids. In comparison to the baseline SA model, it shall "be passive to the original model in well-resolved flowfields and should produce negligible differences in most cases." [3]. The SA model, introduces an additional transport PDE for the transported turbulence variable  $\tilde{v}$  to eq. 2.3. The transport equation including the additional transport equation can be formulated as

$$\nabla \cdot \mathcal{F}^C(\mathbf{u}) - \nabla \cdot \mathcal{F}^V(\mathbf{u}, \nabla \mathbf{u}) - S(\mathbf{u}, \nabla \mathbf{u}) = \frac{\partial \mathbf{u}}{\partial t} \quad (2.4)$$

with a vector of conserved variables

$$\mathbf{u} = \begin{bmatrix} \rho \\ \rho v_1 \\ \rho v_2 \\ \rho v_3 \\ \rho E \\ \rho \tilde{v} \end{bmatrix} \quad (2.5)$$

Compared to equation 2.3, an additional source term  $S$  is present in the equation, which only acts on the production of  $\rho \tilde{v}$ . The exact definition for the fluxes of the turbulent variable equation can be found in [45] and [3].

## 2.2. Orthonormal basis DG formulation

To find a solution to the aforementioned PDEs, the equations need to be discretized in space and time. For the spatial discretization, an orthonormal basis discontinuous Galerkin method is used in this study [32].

Consider the domain  $\Omega$  with boundary  $\Gamma$ , covered by a conformal mesh. The solution of the PDE is defined on each element, using element-local polynomials up to a total degree of  $k$  for a method of order  $k+1$ . The basis functions  $\phi_j \in \mathbb{P}_j^M$  are chosen such that  $\langle \phi_i, \phi_j \rangle = \delta_{ij}$ , where  $\delta_{ij}$  is the Kronecker delta. This orthonormal basis is formulated in physical space and centred on the centroid of the element [8]. This basis spans the same polynomial space as the Taylor basis used by Luo et al. [38, 33]. Compared to a Taylor basis, the mass matrix of this orthonormal basis is the identity matrix and thus results in a well-conditioned linear system [8]. This choice of basis furthermore enables the use of agglomeration-based multigrid methods to accelerate the solution process[7]. The numerical solution  $\mathbf{u}_h$  on the element  $i$  is given by

$$\mathbf{u}_h^i = \sum_j w_j^i \phi_j^i \quad (2.6)$$

The goal of the DG method is to find a numerical solution  $\mathbf{u}_h$ , which satisfies the PDE of interest in a weak sense under appropriate test functions  $\psi$ . The test functions  $\psi$  used are the same as the basis functions  $\phi$  of the method. To simplify the expressions, the time derivative of the equation is dropped.

$$\sum_i \int_{\Omega^i} \psi \left( \nabla \cdot \mathcal{F}^C(\mathbf{u}_h^i) - \nabla \cdot \mathcal{F}^V(\mathbf{u}_h^i, \nabla \mathbf{u}_h^i) \right) d\Omega = \sum_i \int_{\Omega^i} \psi S(\mathbf{u}_h^i, \nabla \mathbf{u}_h^i) d\Omega \quad (2.7)$$

This can be simplified by using integration by parts to yield the following.

$$\sum_i \int_{\Gamma^i} \psi \left( \mathcal{F}^C(\mathbf{u}_h^i) - \mathcal{F}^V(\mathbf{u}_h^i, \nabla \mathbf{u}_h^i) \right) d\Gamma - \sum_i \int_{\Omega^i} \nabla \psi \cdot \left( \mathcal{F}^C(\mathbf{u}_h^i) - \mathcal{F}^V(\mathbf{u}_h^i, \nabla \mathbf{u}_h^i) \right) d\Omega = \sum_i \int_{\Omega^i} \psi S(\mathbf{u}_h^i, \nabla \mathbf{u}_h^i) d\Omega, \quad (2.8)$$

where  $\Gamma_i$  is the boundary of element  $i$ , including both boundary and inner faces. As the state at the element boundaries is discontinuous, proper numerical fluxes  $F^C$  and  $F^V$  have to be defined.

<sup>1</sup><https://how5.cenaero.be/>

## 2.3. Inviscid flux computation

To ensure the stability of the convective fluxes, Roe upwinding is used [28]. For this, the convective numerical flux at the integration point in question is calculated as

$$F^C = \frac{1}{2} (\mathcal{F}^C(\mathbf{u}_h^+) + \mathcal{F}^C(\mathbf{u}_h^-) - |A_{Roe}|(\mathbf{w}_h^+ - \mathbf{w}_h^-)). \quad (2.9)$$

The superscripts + and – indicate the different sides of the face of interest. As Roe's method has no way of distinguishing between compressive and expansive shocks, the method itself admits nonphysical solutions. To alleviate this nonphysical destruction of entropy, Harten introduced an entropy fix to the method [23]. The strength of this entropy fix is controlled by the entropy fix fraction parameter. This entropy fix fraction is kept at 10% of the maximum eigenvalue for all test cases.

## 2.4. Viscous flux computation

From equation 2.7 it can be seen that the computation of viscous fluxes involves the gradient of the state in addition to the state itself. To obtain the derivative of the state, the basis functions of the elements can be differentiated. These element-local derivatives of the basis functions will, however, be of a lower order than the state itself. For a  $DG(P1)$  method, the gradients would only be represented as a constant over the element. Since for a second-order method, a second-order gradient is needed on each element and each face, the resulting method would not be second order. Furthermore, such a naive treatment of viscous effects would not take into account the discontinuities of the solution over the element faces. To alleviate this special viscous treatments are used in DG methods. There are several approaches proposed in literature to deal with viscous problems in DG methods, such as the local discontinuous Galerkin (LDG) method [15] and the symmetric interior penalty (SIPG) method [24]. In the present code, the BR1 [5] and BR2 [9] schemes by Bassi and Rebay are used.

### 2.4.1. BR1 scheme

The BR1 scheme was first proposed by Bassi and Rebay in [5] for the solution of the Navier-Stokes equations. In the scheme, a local lifting operator  $\mathbf{r}$  is defined for every face  $\sigma$  of the element  $\Omega_\sigma$ . The lifting contribution is defined in the space of the basis functions of the element. For the computation of the lifting operator the jump over the face  $[[u_h]] = u_h^+ \mathbf{n}^+ + u_h^- \mathbf{n}^-$  is introduced.

$$\int_{\Omega_\sigma} \mathbf{r}_\sigma ([[u_h]])_\sigma \cdot \psi \, d\mathbf{x} = - \int_\sigma \frac{\psi}{2} \cdot [[u_h]]_\sigma \, d\sigma \quad (2.10)$$

for all test functions,  $\psi$  is defined on the element. The local lifting operators of all faces of an element are then used to define a global lifting operator for the element.

$$\mathbf{R}([[u_h]]) = \sum_{\sigma \in \Sigma} \mathbf{r}_\sigma ([[u_h]]) \quad (2.11)$$

This global lifting operator provides an additional gradient component for the computation of fluxes over the faces and inside the element.

$$\mathcal{F}^V(\mathbf{u}_h, \nabla \mathbf{u}_h + \mathbf{R}([[u_h]])) \quad (2.12)$$

As the computation of the flux over a face includes all faces of both cells, the BR1 scheme is not compact, as second-order neighbours of the element are involved in the computation [10]. This non-compact property leads to stiffer numerical systems, as well as requiring additional computational effort in deriving the exact Jacobian matrix of the scheme. Furthermore, Arnold et al. show, that the BR1 scheme is not unconditionally stable for purely elliptic problems [4]. These properties make the scheme itself undesirable in external aerodynamics, and its use remains limited.

### 2.4.2. BR2 scheme

A modification to the BR1 scheme yields the second scheme of Bassi and Rebay (BR2), which was first proposed in [6, 9]. This scheme is similar to the previously mentioned BR1 scheme in the sense, that a local lifting operator is defined on each face, as well as the summation of these local lifting contributions to a global lifting for the cell. The differences however arise in the usage of these lifting operators. In the BR2 scheme, only the local lifting contribution of a face (eq. 2.10) is used for the flux computation over the face. For the inner-element flux computation, the global lifting operator is used as in the BR1 scheme, as can be seen in equation

2.12. With this modification, only the neighbouring elements of a face are used for the flux evaluation over the face, resulting in a compact method.

To emulate the missing influences of the other faces on the flux computation using the local lifting contribution, a penalty parameter  $\eta$  has been introduced by Brezzi et al. [11].

$$\mathcal{F}^V(\mathbf{u}_h, \nabla \mathbf{u}_h + \eta \mathbf{r}_\sigma([\![\mathbf{u}_h]\!]]) \quad \text{for faces} \quad (2.13)$$

The standard value for  $\eta$  arising from the previous justification is the number of faces of the cell. Brezzi et al. show, that this method is stable for all  $\eta \geq n_f$ , where  $n_f$  is the number of faces of the element [11]. In the original BR1 formulation, faces only contribute to the additional gradient in the direction of their normal vector. Thus, it can be argued, that  $\eta = 2$  is a reasonable choice for regular hexahedral meshes. The influence of this penalty parameter on the error behaviour of the method will be discussed in section 5.4.2.

The BR2 scheme has been shown to be more stable than the BR1 scheme [4] and its Jacobian can be formulated using only the direct neighbours of the cell. Due to these properties, the scheme has been widely used for external aerodynamics [34, 7] and will be used for the remainder of the document unless specifically mentioned otherwise. A more detailed analysis of viscous schemes for DG methods can be found in [1, 2] by Alhawwary et al.

# 3

## Reconstructed Discontinuous Galerkin

The reconstructed discontinuous Galerkin (rDG) method was first proposed by Dumbser et al. [19, 18] as DG  $P_M P_N$  methods for hyperbolic equations. The method has since been applied to compressible flows in [16] by Dumbser et al. The method has been further adapted by Luo et al. in [38, 39, 36, 34, 37], which introduce the term reconstructed discontinuous Galerkin method, in this study.

This chapter aims to introduce the rDG method as well as two different reconstruction techniques. Furthermore, a clear distinction is made between existing approaches in the literature and novel extensions to the methods. Finally, a short review of test cases to which rDG methods have successfully been applied will be given.

The general formulation of the method will be presented in section 3.1, along with the viscous treatment in rDG methods. Two different reconstruction approaches will be introduced in section 3.3. Finally, an overview of test cases, to which the rDG method has successfully been applied will be presented in section 3.4.

### 3.1. Preliminaries

The reconstructed discontinuous Galerkin method aims to unify higher-order finite volume methods and discontinuous Galerkin methods [19], thus both methods are represented in the limits of the method. A rDG( $P_0 P_N$ ) method is equivalent to a higher-order finite volume method of order  $N + 1$ , while the methods belonging to the family of rDG( $P_M P_M$ ) are classical discontinuous Galerkin methods of order  $M + 1$ . However, all methods that do not fall onto these limits are novel methods [19]. A visualisation of the distribution of these methods can be seen in figure 3.1.

As in discontinuous Galerkin methods, the solution is represented using element-local polynomials of up to degree  $N$  for a method of order  $N + 1$ . The basis functions used are the same as previously described in section 2.2

$$\{\phi_j\} = \mathbb{P}^M \quad (3.1)$$

Similar to finite volume methods, a higher order state is reconstructed from the represented state  $\mathbf{u}_h$  using element-local polynomials up to order  $N$ , for  $N > M$ .

$$\{\phi_{jR}\} = \mathbb{P}^N \quad (3.2)$$

The reconstructed solution can then be defined by a linear combination of these extended basis functions.

$$\mathbf{u}_R^i = \sum_j v_j^i \phi_{jR}^i \quad (3.3)$$

To efficiently increase the order of the numerical solution, the basis shall be nested, such that only the additional degrees of freedom need to be calculated and the underlying degrees of freedom do not change [19, 18]. The orthonormal modal basis by Bassi et al. [6], which is used in this study, satisfies this requirement.

$$\{\phi_j\} \subset \{\phi_{jR}\} \quad (3.4)$$

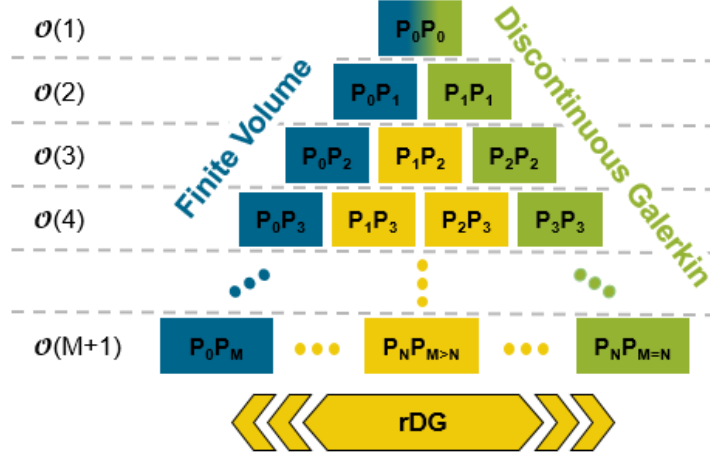


Figure 3.1: "Classification of the proposed  $P_N P_M$  schemes. The leftmost branch ( $N=0$ ) coincides with standard finite volume schemes and the rightmost branch ( $N=M$ ) with classical DG schemes. From third-order on, there is a new class of intermediate schemes in between those branches." Figure adapted from [19]

The reconstructed state  $\mathbf{u}_R^i$  in the element  $i$  is then used in place of the represented state to compute the fluxes and sources in the discretization such that equation 2.7 is modified to yield

$$\sum_i \int_{\Omega^i} \psi \left( \nabla \cdot \mathcal{F}^C(\mathbf{u}_R^i) - \nabla \cdot \mathcal{F}^V(\mathbf{u}_R^i, \nabla \mathbf{u}_R^i) \right) d\Omega = \sum_i \int_{\Omega^i} \psi S(\mathbf{u}_R^i, \nabla \mathbf{u}_R^i) d\Omega \quad (3.5)$$

An example of such a reconstructed state compared to the exact analytical solution and the underlying DG representation can be found for the example of an rDG(P1P2) method in figure 3.2. The example utilises a least-squares reconstruction, which will be explained in detail in section 3.3.1 It should be noted that the test functions are the same as for the underlying DG method, and thus the resulting numerical system is of the same size as of the underlying DG method [16]. As the order of accuracy depends on the reconstructed state, this however, results in a smaller numerical system for the same order of accuracy than for a native DG method. Dumbser et al. showed in [18], that the linear stability limit for rDG methods depends solely on the underlying DG method and not on the order of the reconstruction. This decrease in the size of the numerical system for a given order and the increased stability margin may lead to a decrease in computational effort compared to native DG methods.

Furthermore, it can be argued that to properly solve equation 3.5 numerically, one must be able to integrate polynomials of degree  $N+M$  exactly [35]. This degree of integration will not exactly integrate the numerical fluxes which depend on a non-linear combination of the conserved variables. However, every degree lower can be expected to not yield the correct solution even for linear fluxes. In comparison to this, a discontinuous Galerkin method with comparable order of accuracy needs to at least integrate polynomials of degree  $2 * M$  exactly [35]. If the integration is done using the optimal Gauss-Legendre quadrature, the nodes needed for a subset of rDG methods are shown in figure 3.3. From the figure it can be seen that increasing the order of all DG methods by 1 does not increase the number of Gauss points needed, which can be proven by looking at the expression for the exactly integrated polynomial degree for the number of nodes used in the Gauss quadrature  $p = 2n - 1$ . As  $2 * M$  is always even, the Gauss-Legendre rule used is of one order higher than the minimum degree needed. When comparing the number of integration points needed for rDG methods, it can be seen that they are always less than the number of points needed for a DG method of the same order. For the evaluation of the residual, the solution needs to be computed at each integration point. Thus, fewer evaluations of the basis functions are needed, reducing the computational effort.

### 3.2. Viscous flux computation in reconstructed DG methods

Even though the reconstruction in rDG methods provides a coupling between discontinuous elements, the analytical element-wise derivative is still one order lower than required for an order  $M+1$  method. Thus, the viscous treatments mentioned above need to be used. For this, the lifting operator is formulated in the space of reconstructed polynomials. For this, in equation 2.10, the test functions are chosen as the basis functions of the reconstructed polynomial state. This approach was introduced by Luo et al. [38] and treats

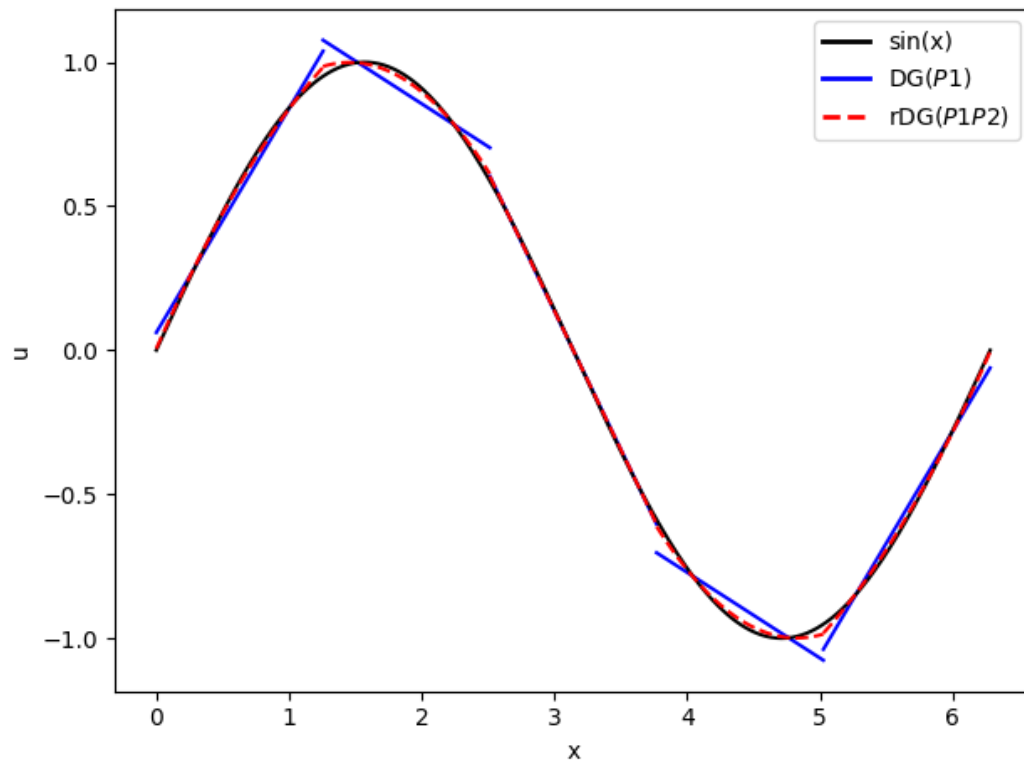


Figure 3.2: Comparison of the discretization for a sine wave between a DG( $P_1$ ) (blue) and a rDG( $P_1P_2$ ) method (red). The exact sine wave is shown in black.

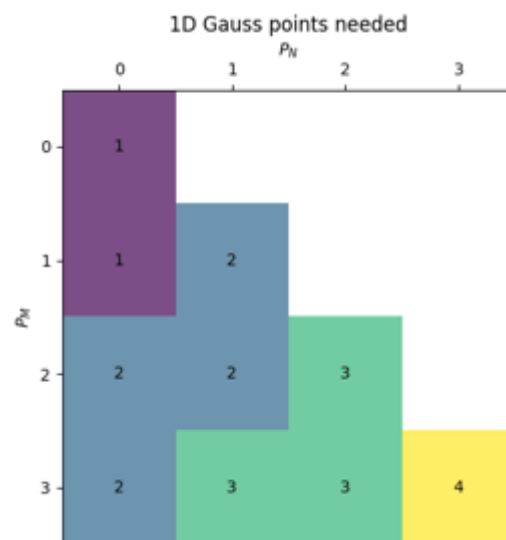


Figure 3.3: Number of Gauss quadrature points needed in 1 dimension for a selection of rDG methods

both reconstructed and underlying degrees of freedom the same. Furthermore, this approach does not yield the same viscous fluxes for a method using a no-op or constant reconstruction, where the additional degrees of freedom are kept to zero. Both of these factors may affect the accuracy of the viscous treatment compared to native DG methods.

### 3.3. Reconstruction methods

The reconstructed solution is formed by applying a reconstruction operator  $R$  to the numerical solution  $\mathbf{u}$ . In general, the reconstruction shall be conservative, such that

$$v_j^i = w_j^i; \quad \forall i \in \{1, 2, \dots, N\}. \quad (3.6)$$

This ensures all represented degrees of freedom are preserved in the reconstructed state. Applying this condition to an rDG( $P_M$   $P_M$ ) method yields a reconstruction operator which is the identity matrix, and thus recovers the underlying DG method.

#### 3.3.1. Least-squares Reconstruction

In the original papers by Dumbser et al. [19, 18, 16] a least-squares reconstruction technique is introduced, which is based on solving a local constrained least-squares problem on each cell. For the reconstruction, the basis functions of cell  $i$  are extended over the whole Stencil  $S_i$ , which includes  $n_e$  Elements. The condition is formulated such that the reconstructed state of cell  $i$  is indistinguishable from the solution on the elements of the stencil in a weak sense, for all test functions  $\phi^j$ . This can be formulated as

$$\langle \phi_{j_R}^i, u_R^i \rangle_{E_k} = \langle \phi_{j_R}^i, u^j \rangle_{E_k}; \quad \forall E_k \in S_i, \quad (3.7)$$

This reconstruction is well-posed, if the Stencil  $S_i$  contains at least  $\frac{L_N}{L_M}$  elements, where  $L_N$  and  $L_M$  are the number of degrees of freedom per element for the reconstructed and represented solution respectively [19, 18]. This limit is purely theoretical based on the well-posedness of the reconstruction problem. In practice, a higher number of elements is desirable for the accuracy and stability of the method [19, 37]. From this relationship, it can be seen that the number of stencil elements needed for methods with  $N > 0$ , is significantly lower than for a comparable higher-order finite volume method. For the stencil, two different choices are considered. The standard least-squares reconstruction method utilises a compact stencil, which only includes the von Neumann neighbourhood of the cell of interest [38, 39, 34]. This choice of stencil suffers from the same linear instability on tetrahedral meshes as encountered in second-order finite volume methods [22]. This linear instability can be resolved by using weighted essentially non-oscillatory (WENO) schemes [35, 52]. These schemes use the reconstructed polynomials of adjacent cells as biased stencils. The weighting of these stencils is done by evaluation of an oscillation indicator proposed by Dumbser [17]. Due to their high non-linearity, WENO schemes are hard to differentiate exactly and lead to stiff numerical systems. This leads to stalling convergence for even simple test cases, as shown by Xia et al. [51] and Liu et al. [31, 30].

**Extended Stencil** Another solution to the linear instability of a face-based neighbourhood stencil is to include more cells in the stencil. For this, all cells sharing a vertex with the cell of interest are included in the stencil. This increases the number of elements in the stencil and increases the number of directions from which information is included. A comparison between the extended stencil and the compact stencil variant can be seen in figure 3.4. Extension of the stencil might also increase the accuracy of least-squares based finite volume methods in cell-centred codes compared to vertex-centred codes, as has been noted by Schwöppe and Diskin in [43].

**Boundary Conditions** From equation 3.7, it can be seen that the state needs to be defined in all cells of the stencil. This poses a problem for cells which include a boundary face. The boundary conditions on the equation are imposed such that the exterior state at the boundary faces is known. However, as higher-order methods generally need curved meshes to reach their designed order of accuracy [6], no general formulation for a ghost cell can be found. To avoid this problem, equation 3.7 is reformulated on boundary faces to

$$a_{\Gamma_i} \langle \phi_{j_R}^i, u_R^i \rangle_{E_k} = a_{\Gamma_i} \langle \phi_{j_R}^i, u^j \rangle_{\Gamma_i}, \quad (3.8)$$

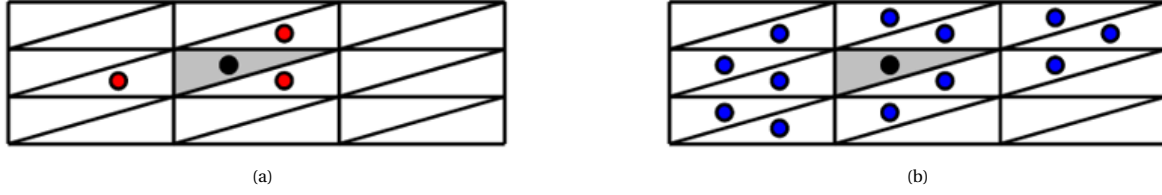


Figure 3.4: (a) Compact face-based stencil on the example of a structured triangular mesh. (b) Extended node-based stencil on the example of a structured triangular mesh. From [43]

where  $\Gamma_i$  is the boundary face of cell  $i$ . In order to make this consistent with previous formulation, a factor

$$a_{\Gamma_i} = \frac{V_i}{A_{\Gamma_i}}$$

is introduced, where  $V_i$  is the volume of cell  $i$  and  $A_{\Gamma_i}$  is the area of the boundary face  $\Gamma_i$ .

**Normal equation formulation** To solve the over-constrained system arising from equation 3.7, a least-squares method is used. For this a cost function  $f^i$  is formulated for each cell  $i$ , where  $\mathbf{v}_a^i = \{u_n^i\}$  for  $N_{DOF} < n \leq M_{DOF}$  is the vector of additional reconstructed states

$$f^i(\mathbf{v}_a^i) = \sum_{k=0}^{n_e} \left( \langle \phi_{j_R}^i, u_{R_k}^i \rangle_{E_k} - \langle \phi_{j_R}^i, u^j \rangle_{E_k} \right)^2. \quad (3.9)$$

This can be split up to yield

$$f^i(\mathbf{v}_a^i) = \sum_{k=0}^{n_e} \left( \langle \phi_{j_R}^i, u^i \rangle_{E_k} + \langle \phi_{j_R}^i, \sum_{n=N_{DOF}+1}^{M_{DOF}} v_n^i \phi_{n_R} \rangle_{E_k} - \langle \phi_{j_R}^i, u^j \rangle_{E_k} \right)^2. \quad (3.10)$$

From this it can be seen that only the middle inner product is dependent on  $\mathbf{v}_a$ , while all other terms depend on the represented known state. To solve this least-squares problem, the minimum of  $f$  needs to be found. For this the derivative of  $f$  with respect to  $\mathbf{v}_a$  needs to be found. This leads to a linear system  $A\mathbf{v}_a = b$  for each cell of size  $M_{DOF} - N_{DOF}$ . The matrix  $A$  of the system is solely dependent on the mesh metric and can thus be constructed and inverted once. The vector  $b$  collects all terms, which depend on the current represented state.

**Inverse distance weighting** Mavriplis [40] shows that the least-squares formulation for finite volume meshes can be inexact in regions with highly anisotropic cells, such as in boundary layers. He proposes an inverse distance weighting in the least-squares formulation, and shows that this method can reconstruct gradients with higher accuracy in boundary layers. This can be adapted to rDG methods, by introducing a weighting term into equation 3.9.

$$f^i(\mathbf{v}_a^i) = \sum_{k=0}^{n_e} w_i^k \left( \langle \phi_{j_R}^i, u_{R_k}^i \rangle_{E_k} - \langle \phi_{j_R}^i, u^j \rangle_{E_k} \right)^2, \quad (3.11)$$

where  $w_i^k$  is the weighting for cell  $k$  for the reconstruction in cell  $i$ . The weighting is calculated such, that cells closer to the original cell receive a higher weighting than cells further away. The formulation for the weighting function is chosen as

$$w_i^k = \frac{1}{\|\mathbf{x}_i - \mathbf{x}_k\|^n}, \quad (3.12)$$

where  $n$  is an exponent greater or equal to 0 and  $\mathbf{x}_i$  is the centroid of element  $i$ . If it is 0, no inverse distance weighting is performed. An exponent of 1 yields the most accurate solutions for finite volume methods.[40] The influence of this weighting on the stiffness of the reconstruction problems can be found in Appendix A.

### 3.3.2. Variational Reconstruction

Variational reconstruction was first introduced for  $k$ -exact finite volume methods. In this technique, the goal is to find the coefficients of the reconstructed solution such that some cost function over the domain is minimised. The cost function chosen to be minimized in [50] is the total interfacial jump integration (IJF), which

is a measure of the discontinuity of each spatial derivative over the element interfaces. The total interfacial jump integration is defined as the sum of all interfacial jumps  $I_f$ . The Interfacial jump integration for a rDG(P1P2) method in two dimensions for a Taylor DG method is given in equation 3.13, where  $d_{lr}$  is the distance between the cell centroids and  $u_R^r$  and  $u_R^l$  are the right and left hand reconstructed states respectively [53].

$$I_f = \frac{1}{d_{lr}} \int_f \sum_{m=0}^2 \sum_{n=0}^m \left( \frac{1}{m!} \frac{\partial^m u_R^l}{\partial x^n \partial y^{m-n}} d_{lr}^m - \frac{1}{m!} \frac{\partial^m u_R^r}{\partial x^n \partial y^{m-n}} d_{lr}^m \right)^2 d\Gamma. \quad (3.13)$$

$$I = \sum I_f. \quad (3.14)$$

The goal of the method is then to minimize  $I$  with respect to the additional reconstructed states. This leads to a global linear system of the form  $Ax = b$ , where  $A$  is dependent only on the mesh and  $x$  is the column vector of all additional degrees of freedom for a conservative variable. The right-hand side  $b$  is a function of  $\mathbf{u}$  and thus changes for every non-linear iteration. Wang et al. [50], show that the resulting matrix is symmetric and positive definite and as such is not only solvable but enables the use of more specialised linear solvers such as the conjugate gradient (CG) method. The linear system does not need to be solved exactly at each non-linear iteration and an approximate solution is sufficient as the reconstruction converges in parallel to the non-linear flow problem.

As the method only involves integrals over boundaries, the treatment of boundary conditions is simplified compared to the least-squares reconstruction. Furthermore, the method involves only direct face neighbours for the construction of the linear system and thus the method can be classified as compact even though the stencil of the method is the entire mesh implicitly [13]. This implicit global stencil removes the linear instability present in the least-squares reconstruction [29]. Wang et al. [50] show that for the one-dimensional case of an FV method for the linear advection equation, variational reconstruction (VR) offers superior spectral properties compared to a compact least squares (CLS) reconstruction of comparable order.

**Convergence strategies for complex flows** This global linear reconstruction problem needs to be solved completely at the end of the non-linear iteration process to yield its formal order of accuracy. However, as the non-linear flow problem and the linear reconstruction problem are only weakly coupled to preserve the advantageous properties of rDG methods, this can lead to diverging behaviour. For complex test cases, it is furthermore not possible to solve the linear reconstruction problem exactly at every iteration, as this leads to a very stiff numerical system. To deal with this, the linear reconstruction problem is only solved partially at each non-linear iteration starting from a zero vector. This approach avoids the divergence problems encountered if the non-linear problem changes faster than the linear reconstruction problem. A drawback of this approach, however, is that the method is not formally of the correct order.

### 3.4. State of the art

To formulate research questions, that achieve the previously defined research objective, the state of the art for rDG methods will be laid out in sections 3.4.1 and 3.4.2. Afterwards, the research questions for this study are defined.

#### 3.4.1. Least-squares Reconstruction

In [38, 39, 34, 35, 37], Luo et al. show that the least squares reconstruction technique can reach the expected order of accuracy and performs better in terms of error per degree of freedom for the Euler equations for two-dimensional test cases on purely hexahedral grids. Cheng et al. show in [14], that the accuracy of rDG methods deteriorates on hybrid two-dimensional grids for the Euler equations. They furthermore show that the least-squares rDG method does not perform as well as a native DG method for low Reynolds number viscous flows. However, they show that the rDG method can run significantly faster than a higher-order DG method on the same grid. Liu et al. [31, 30] apply the least-squares reconstruction method to two-dimensional airfoil flows at a Reynolds number of  $10^4$  and show that the method converges, although no comparisons to other higher-order methods are given. In [30] the authors try to compute a three-dimensional Hemisphere test-case, at a moderate Reynolds number of  $3.5 \times 10^5$ . However, the residual could not be reduced from DG(P1) initial solution.

### 3.4.2. Variational Reconstruction

Li et al. [29] show that it performs similar to least-squares reconstruction in terms of error. In later papers by Cheng et al. [13], this is confirmed for the inviscid flow over the smooth bump. They furthermore show that variational reconstruction performs similar to least-squares reconstruction for low Reynolds number flows ( $Re = 100$ ) in two dimensions. However, both methods perform worse than a DG method of comparable order in terms of error per degree of freedom. Zhang et al. [53] apply variational reconstruction to the zero pressure gradient flat plate, for which it performs marginally better than the least-squares reconstruction. However, all rDG methods were found to perform worse than a third-order DG method in terms of degrees of freedom.

### 3.4.3. Research questions

In previous papers, the performance of rDG methods decreases for viscous flows compared to inviscid flows. As in RANS simulations, large viscous contributions to the solution can be found in boundary layers, the effect of the viscous treatment on the accuracy of rDG methods is subject of the first research question.

**RQ1:** *How does the viscous treatment affect the discretization error and linear stability of rDG methods?*

In section 3.3.1, an inverse-distance weighting was adapted from finite volume methods. As meshes used for RANS simulations often exhibit highly anisotropic regions in boundary layers, the effect of this inverse distance weighting for anisotropic boundary layer meshes will be evaluated for the second research question

**RQ2:** *To which extent can inverse-distance weighting in least-squares reconstruction decrease the spatial discretization error of rDG methods in highly anisotropic mesh regions, such as boundary layers?*

The third research question aims to answer the main topic of the research objective. For this, the two different rDG methods will be applied to different two and three-dimensional test cases at high Reynolds numbers.

**RQ3:** *How do rDG methods perform in terms of error per degree of freedom and error per unit of computational effort for High-Reynolds number flows in two and three dimensions?*

The last research question aims to address the reported difficulties in convergence for rDG methods for high Reynolds number flows. For this, the allowable simplifications in the Jacobian matrix will be evaluated for different flow equations.

**RQ4:** *How do simplifications in the construction of the Jacobian affect the convergence of steady-state simulations?*



# 4

## Non-linear solution process

This chapter will explain the non-linear solver used for this study. First, the discretization of the equations in pseudo time will be introduced in section 4.1. This section will furthermore introduce the fully implicit linearized backwards Euler method used for this study. The solution procedure for the arising linear systems will be discussed in section 4.2. This section will furthermore introduce the linear solver stack and explain the different approaches for approximating the Jacobian used in this thesis.

### 4.1. Discretization in pseudo time

In the previous chapter, the PDE was transformed into semi-discrete form:

$$R(\mathbf{u}) = \mathbf{R} = \overline{M} \frac{\partial \mathbf{u}}{\partial t}, \quad (4.1)$$

where  $\mathbf{R}$  is the residual vector and  $\overline{M}$  is the mass matrix of the basis functions. To arrive at a converged solution for the problem, the residual of  $\mathbf{u}$  should be 0. For a linear operator  $R$ , this can be done by a simple linear solution. As for the Euler and RANS-SA<sub>neg</sub> equations, however, the residual operator is not linear, the solution to the equation needs to be found in another way. One way is to use the inherent time dependence of the solution, to step forward in time until a steady-state solution is found. As only the steady state solution is of interest, the order of accuracy of the time-stepping method used is irrelevant.

#### 4.1.1. Linearized implicit Euler

In the linearized implicit Euler method, the next iteration of the solution is calculated as

$$\left[ \frac{\overline{M}}{\alpha_i \Delta t} + \overline{J} \right] (\mathbf{u}_i - \mathbf{u}_{i-1}) = \mathbf{R}_i, \quad (4.2)$$

where  $\overline{J}$  is the linearized Jacobian matrix of the residual. The pseudo timestep  $\alpha_i \Delta t$  is chosen locally for each cell based on the local CFL number and a factor  $\alpha_i$ . For  $\alpha_i \rightarrow \infty$ , the linearized backwards Euler method converges towards a Newton-Raphson method. The solution to this linear system does not need to be exact, as the formal order of the time-stepping method does not influence the final converged solution.

#### 4.1.2. Switched evolution relaxation

The local CFL factor  $\alpha_i$  is chosen based on the non-linear residual of the cell. For this, a switched evolution relaxation (SER) ramping devised by Mulder et al. [41] is used. The factor  $\alpha_i$  is calculated as

$$\alpha_i = \left( \frac{\mathcal{R}_0}{\mathcal{R}_i} \right)^n \quad (4.3)$$

where  $\mathcal{R}$  is some norm of the residual. The exponent  $n$  controls the speed of the ramping. One can see, that if the Residual norm  $\mathcal{R}_i$  approaches zero, the pseudo timestep will approach infinity and thus recover the Newton-Raphson method. The residual norm is calculated as the  $L_2$  norm of the residual of all transport equations. The exponent is chosen as 0.8 for all two-dimensional test cases and 0.6 for all three-dimensional test cases.

## 4.2. Linear solution process

For the computation of the update in the linearized implicit Euler method, an approximate linear solve is required. As the linear system to be solved is too large to be inverted directly, iterative linear solvers are used.

### 4.2.1. Preconditioned Krylov subspace methods

The linear system is solved using a preconditioned generalized minimum residual (GMRES) solver. The GMRES solver is guaranteed to converge if the matrix  $\bar{A}$  is invertible. To improve the convergence behaviour of the GMRES method, it is preconditioned using a fixed number of Block-Jacobi iterations. The number of preconditioning iterations is chosen based on the polynomial order of the basis functions, to compensate for the increased stiffness of the system. The number of Jacobi iterations for each order of basis functions can be seen in table 4.1. The increase in iterations for increasing polynomial order is needed, as the stiffness of the resulting linear systems increases with polynomial order, and thus a better preconditioner is needed.

Table 4.1: Number of Block Jacobi preconditioning steps for each polynomial order of basis functions.

Polynomial order	Jacobi iterations
1	50
2	77
3	104

To allow the computation of a Block-Jacobi iteration, the diagonal of the matrix needs to be inverted. As the diagonal is not limited to only the blocks on the diagonal of the matrix, a line-based diagonal solver is utilised, which inverts strongly coupled blocks [49]. For the solution of the linear systems, the linear solver library Spliss [48] is used.

### 4.2.2. Usage of approximate Jacobians

For the linearized backwards Euler method, the Jacobian of the Residual needs to be known. For a native DG method using the BR2 scheme, the Jacobian only involves first-order neighbours, and can be calculated exactly in matrix form. For an rDG method, the exact Jacobian does not only involve its direct neighbours but also second-order neighbours, and in the case of the extended stencil, node neighbours. This makes the construction of the exact Jacobian in matrix form very memory intensive.

For the evaluation of a GMRES iteration only the evaluation of the Jacobian with a vector and not the entire Jacobian needs to be known. The matrix-vector product is equivalent to the directional derivative, and thus only one or two, for single-sided and symmetric differencing respectively, evaluations of the residual are needed for each GMRES iteration. Langer et al. showed in [27] that using a GMRES with the aforementioned choice of a finite-difference Jacobian (FD-GMRES) in combination with a Gauss-Seidel preconditioner based on an approximated Jacobian performs very well compared to an LU-SGS linear solver. The experiments in [27] were conducted for a second-order finite volume method, using a Green-Gauss based reconstruction for the gradients required for the viscous flux computation. The approximated Jacobian for the preconditioner is constructed from the underlying finite volume method with no Green-Gauss reconstruction. This is comparable to using the compact Jacobian of the underlying DG method as a preconditioner for a GMRES linear solver, which uses a finite-difference approximation for the directional derivative. It should however be noted that such an approximation introduces a further parameter  $\epsilon$  in the solution process, which controls the step size for the finite difference. The determination of the optimal value for  $\epsilon$  is, however, non-trivial [27]. The need for a finite-difference operation can however be eliminated by leveraging automatic differentiation of the residual around a state. This method provides the exact directional derivative of the residual without the need for determination of an optimal value for  $\epsilon$ .

For this study, two different Jacobians are considered. The first uses the Jacobian of the underlying DG method as an approximated Jacobian. The second uses an exact Jacobian obtained using automatic differentiation. This Jacobian is, however, not formulated in matrix form and will only provide directional derivatives for the GMRES solver. For variational reconstruction, an automatic differentiation Jacobian is not possible, as the linear solver used cannot to be differentiated using AD. Thus a finite-difference Jacobian needs to be used. This, however, requires one or two evaluations of the residual, that each require a partial solve of the underlying linear system of the reconstruction and is thus more expensive than other reconstruction methods.

# 5

## Verification

To prove that the aforementioned variational reconstruction based and least-squares reconstruction based rDG methods were implemented correctly and yield the expected order of accuracy as the mesh is uniformly refined, verification of the implementation is needed. For this, the method of manufactured solutions, which is described in section 5.1, is used. The numerical methods will then be tested using two different PDEs, to separately assess the influence of convective and diffusive fluxes. This is done on the example of the Euler equations in section 5.2 and the RANS-SAneg equations in section 5.3. For each of the equations, three different meshes are used to assess the behaviour of discretization error of the methods with respect to the mesh quality. In addition to a regular hexahedral mesh, a randomly disturbed hexahedral mesh with non-planar faces is used. Furthermore, the methods are tested on an unstructured tetrahedral mesh.

In the final section (5.4), a closer look at the influence of the viscous treatment for rDG methods is presented. For this, two different viscous treatment schemes are compared in their absolute error magnitude. Furthermore, the influence of a user-tunable parameter in the BR2 scheme is investigated. Finally, the linear stability of the viscous treatment in rDG methods is investigated and compared to native DG methods.

### 5.1. Method of manufactured solution

The method of manufactured solutions (MMS) was first proposed by Steinberg and Roache [46] as a numerical procedure to verify the correct implementation of numerical methods. This method is attractive to use for the verification of numerical schemes, as it does not depend on the availability of analytical solutions for the given equation and can be used to verify the discretization on arbitrary meshes.

For the MMS, a solution  $\hat{u}$  of the PDE  $\mathcal{L}(u) = 0$  is defined on the domain  $\Omega$ . However, this solution, in general, does not satisfy the PDE. To fix this, a spatially varying source term  $S$  is defined, such that

$$\mathcal{L}(\hat{u}) + S = 0 \quad (5.1)$$

The source term is calculated analytically, and thus independent of the discretization. It is calculated by propagating the assumed solution  $\hat{u}$  through the PDE. The solution  $u_h$  obtained by solving equation 5.1 using the numerical method of interest can then be used to evaluate the discretization error  $\epsilon$ , by taking the L2 norm of the difference between  $\hat{u}$  and  $u_h$  as shown in

$$\epsilon = \int_{\Omega} (\hat{u} - u_h)^2 d\Omega \quad (5.2)$$

For a vector-valued state  $\mathbf{u}$  of the PDE, this procedure is performed per component.

**Order of accuracy** The order of accuracy of a numerical method is a measure to describe how fast the discretization error of the scheme decreases with isotropic refinement. For a  $n^{\text{th}}$  order accurate method, the discretization error will reduce by a factor of  $k^n$  for an increase in resolution by a factor of  $k$  in every coordinate direction. In a double logarithmic plot of discretization error against the number of degrees of freedom, a  $n^{\text{th}}$ -order method, will appear as a straight line, with slope  $n$ . Verification is performed by confirming that the observed order of accuracy when refining the mesh matches the designed order of accuracy of the method.

**Choice of manufactured solution** Special care must be taken when choosing the manufactured solution  $\hat{u}$ , to collect and observe all error components of the numerical solution. As the discretization error can be explained by the truncation of the Taylor series expansion, a suitable choice for the manufactured solution should include all spatial derivatives. A common choice for such a function are the sine and cosine functions, as they include all spatial derivatives and remain bounded between  $-1$  and  $1$  over the whole domain. Using these functions, a manufactured solution for each component  $\hat{u}_i$  can be assembled as

$$\hat{u}_i = c_i + A_i * \sin(\omega_i^x * x - \phi_i^x) * \sin(\omega_i^y * y - \phi_i^y) * \sin(\omega_i^z * z - \phi_i^z), \quad (5.3)$$

where  $c_i$  is a constant contribution,  $A_i$  is the amplitude of the oscillation,  $\omega_i^k$  is the frequency of the oscillation in the coordinate direction  $k$  and  $\phi_i^k$  is the phase change in the coordinate direction  $k$ . The values chosen for each component are shown in table 5.1. When choosing these parameters, it is important to ensure, that the value of  $\rho$ ,  $\rho E$  and  $\rho \tilde{v}$  are strictly positive over the domain, so that a physical solution exists.

Table 5.1: Parameters chosen for the manufactured solution

Component	$c_i$	$A_i$	$\omega_i^x$	$\phi_i^x$	$\omega_i^y$	$\phi_i^y$	$\omega_i^z$	$\phi_i^z$
$\rho$	1.0	0.15	$0.3 \pi$	$-0.06 \pi$	$0.8 \pi$	$0.74 \pi$	$0.5 \pi$	$-0.05 \pi$
$\rho v_1$	0.2	0.02	$1.0 \pi$	$0.1 \pi$	$0.3 \pi$	$-0.06 \pi$	$0.8 \pi$	$0.26 \pi$
$\rho v_2$	-0.05	-0.0015	$0.6 \pi$	$-0.24 \pi$	$1.0 \pi$	$0.3 \pi$	$0.6 \pi$	$-0.06 \pi$
$\rho v_3$	0.1	0.005	$0.9 \pi$	$0.18 \pi$	$0.3 \pi$	$0.47 \pi$	$0.8 \pi$	$-0.32 \pi$
$\rho E$	3.1	0.93	$0.3 \pi$	$0.56 \pi$	$0.9 \pi$	$-0.225 \pi$	$0.4 \pi$	$0.08 \pi$
$\rho \tilde{v}$	0.01	0.001	$0.2 \pi$	$0.52 \pi$	$0.3 \pi$	$0.06 \pi$	$0.5 \pi$	$-0.05 \pi$

## 5.2. Inviscid flows

The method of manufactured solutions is applied first to the Euler equations, to evaluate the different reconstruction schemes on pure convective problems. This step serves as a baseline for later experiments, as the treatment of inviscid terms does not require additional lifting operators in the context of DG and rDG schemes. The method will first be evaluated on regular hexahedral meshes. A randomly perturbed version of these meshes will also be considered to evaluate the robustness of the numerical methods on meshes with non-planar and non-orthogonal faces.

### 5.2.1. Hexahedral meshes

The method was tested on a mesh cascade of three uniformly refined hexahedral meshes. The randomly perturbed meshes (RPM) were generated by randomly perturbing all interior nodes by up to 20% of the cell size. This was done in a deterministic way so that all equal-sized perturbed meshes are the same between all simulations. The results of the convergence study can be seen in figure 5.1.

From the figure it can be seen that all reconstructed DG methods reach their designed order of accuracy. In terms of absolute error, the standard least-squares reconstruction method performs approximately the same, as the native DG method of the same order. This comparison is done for an equivalent number of degrees of freedom. On the same mesh, the least-squares rDG method will perform worse than a native DG method, due to the increased number of degrees of freedom present in the native DG method. Furthermore, it can be seen that the extended least-squares method performs worse than the standard least-squares method in terms of absolute error. This behaviour will be further investigated in section 5.2.3. The variational reconstruction can be seen to achieve the best performance in terms of error versus degrees of freedom and performs better than the native higher-order DG method on the same mesh.

The dashed lines in the figure indicate the error on randomly perturbed meshes. From these it can be seen that the variational reconstruction is the most sensitive reconstruction to disturbances in the mesh, which is to be expected, as it is the only reconstruction method, which is based on inner face integrals. In section 5.2.4, this behaviour will be evaluated in more depth. In contrast, the standard least-squares reconstruction reduces in accuracy by an amount similar amount to that of the native DG method. The extended least-squares method proves to be resilient to random perturbations in the mesh, as the error does not increase significantly on all three meshes. Even though the error increases for the considered methods on randomly perturbed meshes, all methods retain their designed order of accuracy.

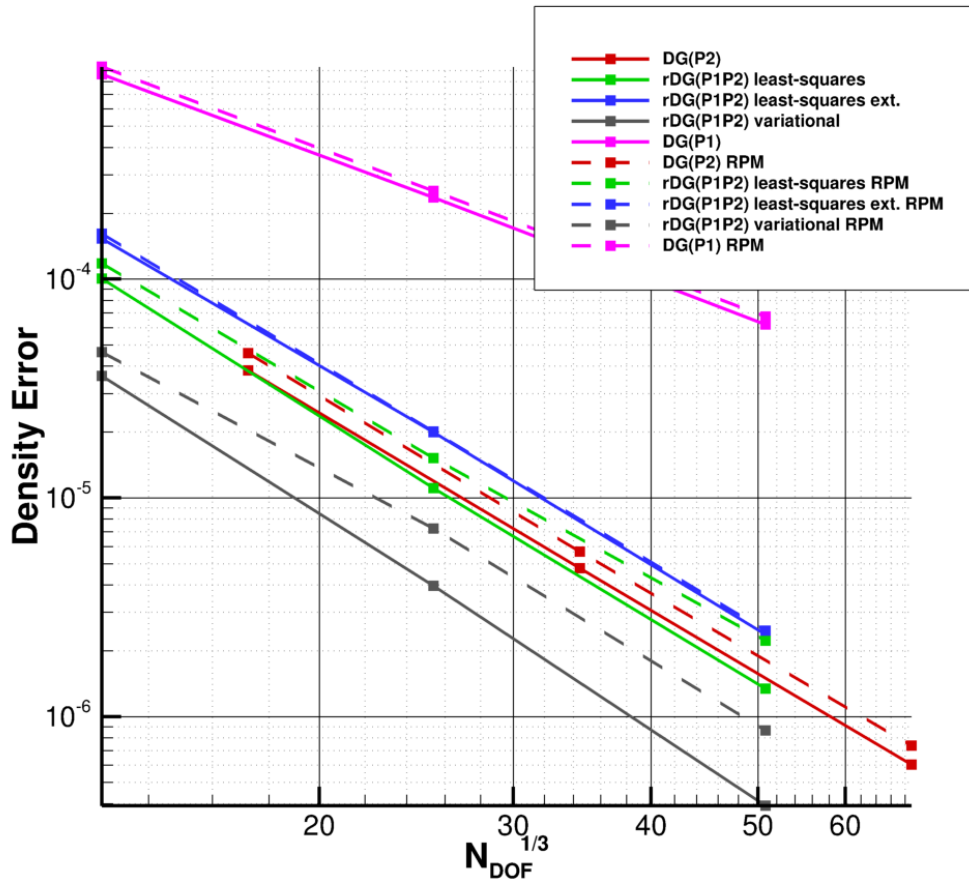


Figure 5.1: Density Error against cube root of the number of degrees of freedom for the method of manufactured solution on a regular and randomly perturbed hexahedral mesh for the Euler equations.

**Solution visualisation** To illustrate the difference between a native DG(P1) method and a rDG(P1P2) method in terms of solution representation, a slice through the solution at  $x = 0$  is presented in figure 5.2. It can be seen, that the rDG(P1P2) method captures the solution better than the underlying DG method. The result of the rDG(P1P2) method is visually very similar to the DG(P2) method.

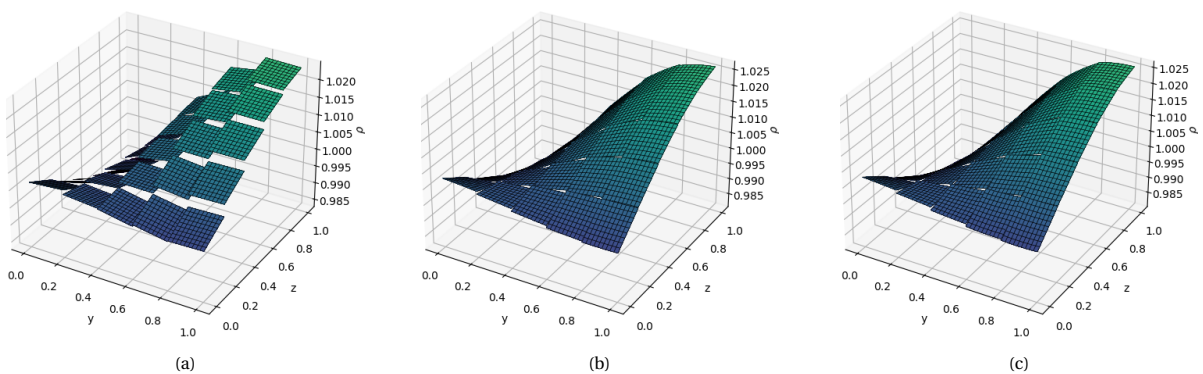


Figure 5.2: Slice through the solution at  $x = 0$  for (a) DG(P1) method, (b) a compact stencil least-squares rDG(P1P2) method and (c) a DG(P2) method.

### 5.2.2. Tetrahedral mesh

The methods was also tested on purely unstructured tetrahedral meshes generated by gmsh[21]. The meshes were not refined by uniform splitting but were generated independently. The results can be seen in figure 5.3.

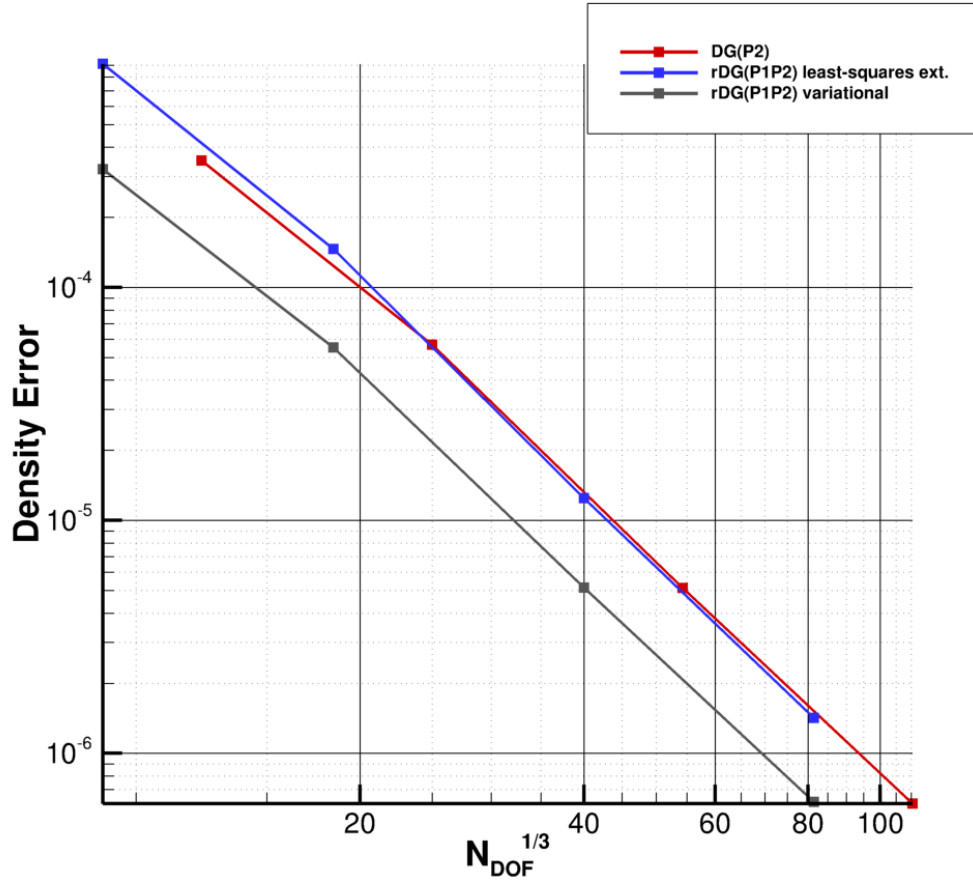


Figure 5.3: Density Error against the number of degrees of freedom for the method of manufactured solution on an unstructured tetrahedral mesh for the Euler equations.

From the figure, it can be seen that all methods reach their designed order of accuracy in between the last 3 meshes of the sequence of consecutively refined meshes. Between the first and second mesh of the cascade, a small deterioration in the order of accuracy can be observed, which might be because the coarsest mesh is too coarse to lie in the region of asymptotic convergence. Furthermore, it should be noted that the standard least-squares reconstruction is not stable on simplicial meshes, and thus no convergence results are presented. This instability is known from least-squares reconstruction in finite volume methods [22]. The least-squares method is stable when using the extended stencil variant, which also includes node neighbours in the reconstruction problem. In terms of absolute error this extended least-squares performs similar to a native higher-order DG method for an equivalent number of degrees of freedom. This is contrary to the findings on the hexahedral mesh, in which the extended stencil variant performed worse compared to the native DG method. The variational reconstruction based rDG method again outperforms the comparable DG method in terms of absolute error per degree of freedom and can reproduce the same accuracy as a DG method on the same grid.

### 5.2.3. Extended stencil on isotropic meshes

As previously noted, the absolute error for the extended least-squares reconstruction is higher compared to the standard least-squares reconstruction. This behaviour comes from the inclusion of 20 additional elements, all of which are located further away from the cell of interest than the original cells of the stencil. To visualise the effect of the additional cells on the reconstruction, figure 5.4 shows the absolute error of the

compact stencil least-squares, the extended least-squares, and an additional least-squares variant which includes only the additional elements in the stencil, due to the inclusion of node neighbours.

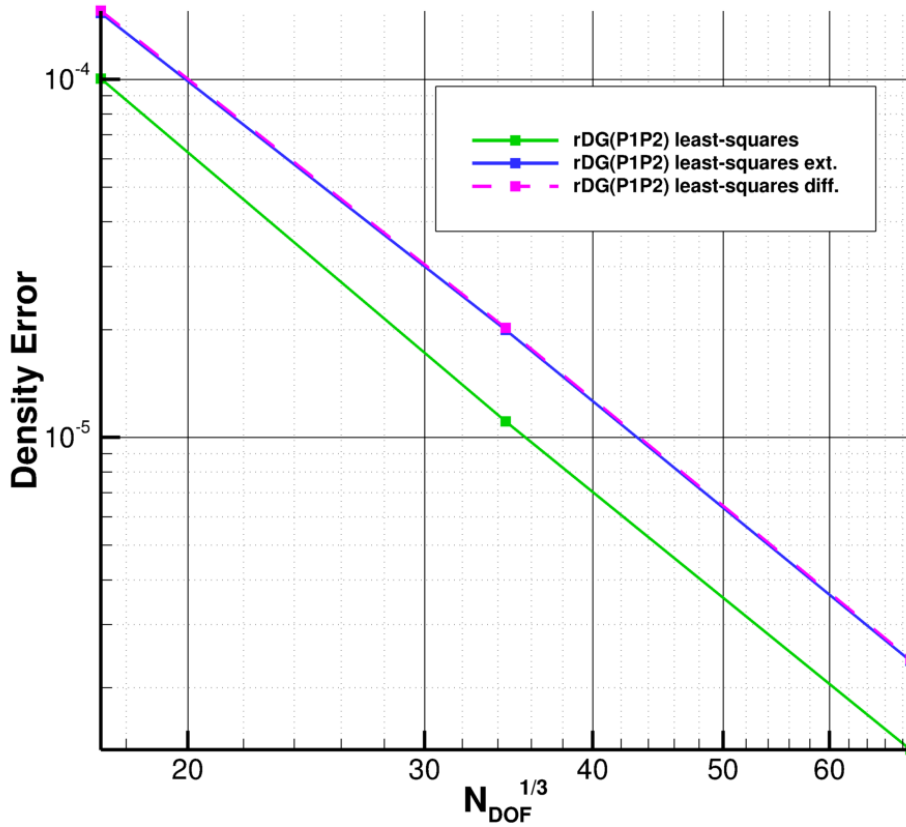


Figure 5.4: Density Error against cube root of the number of degrees of freedom on a regular hexahedral grid for three different stencil choices for a least-squares reconstruction on the example of the Euler equations.

It can be seen that the extended stencil and the stencil only including the additional elements display nearly the same error behaviour. This confirms that the additional elements provide a worse reconstruction than only the face neighbours. As a hexahedron has 20 node neighbours and only six face neighbours, the reconstruction from the node neighbours dominates the least-squares reconstruction problem and thus the full extended stencil does not improve the error on pure hexahedral grids.

#### 5.2.4. Variational reconstruction on non-planar faces

As previously noted, the discretization error in the variational reconstruction increased on the randomly perturbed mesh compared to the DG method. This effect is caused by the non-planar faces in the mesh. As in the randomly perturbed mesh however, the faces are not only non-planar, but are also skewed, the effects of skewed and non-planar faces need to be separated. For this in addition to the randomly perturbed mesh, a purely skewed mesh is generated. For this a parallelepiped with an interior angle of  $5.71^\circ \approx \text{atan}(0.1)$  is meshed with a regular mesh. The inner faces of this mesh are all skewed and are all planar. As this mesh spans a different physical domain, the absolute value of the discretization error will be slightly different compared to the previous meshes. The results can be seen in figure 5.5.

It can be seen, that the purely skewed mesh, does not affect the discretization error for the DG discretization. For the rDG method no negative influence of the skewed mesh can be observed. From this it can be concluded that the deterioration observed for variational reconstruction observed on the randomly perturbed mesh originates from the non-planarity of faces and variational reconstruction performs well on skewed meshes.

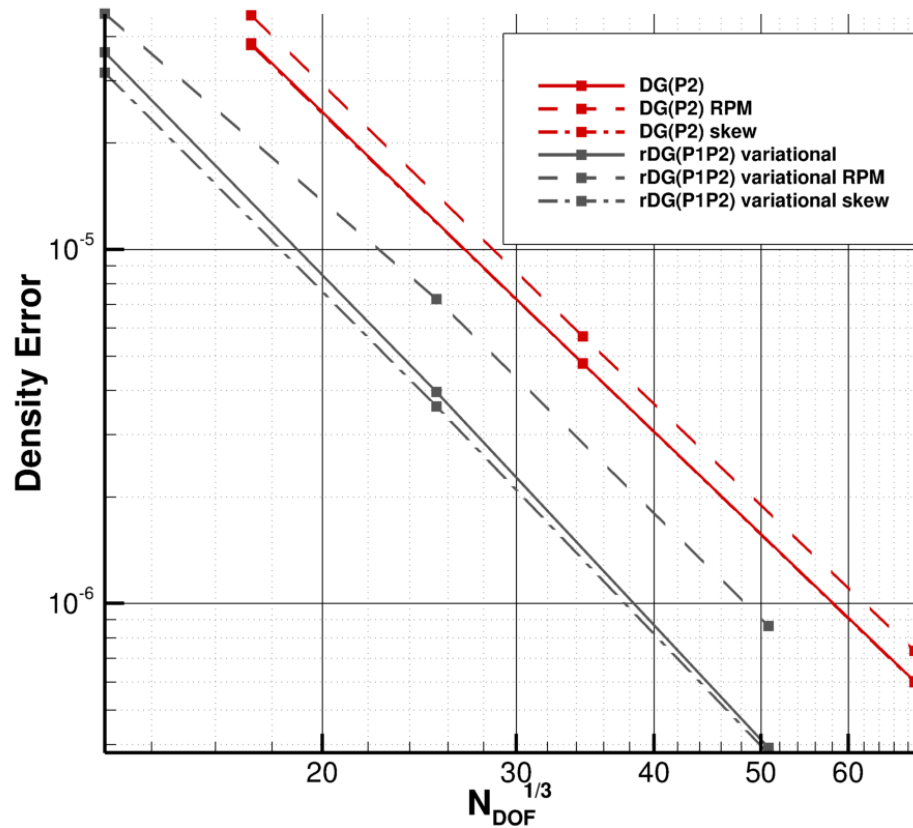


Figure 5.5: Density Error against cube root of the number of degrees of freedom on a hexahedral mesh, a randomly perturbed hexahedral mesh and a parallelepiped mesh.

### 5.3. Viscous flows

In the previous section, the convergence behaviour of rDG methods for purely hyperbolic PDEs was analysed. These equations are treated naturally in DG methods and by extension in rDG methods due to the Riemann problems arising on the element interfaces. For diffusive fluxes, the gradient of the polynomial representation is involved, and thus special schemes are needed to treat viscous problems in the context of rDG methods. For more details on the considered viscous treatments, refer to section 2.4. The BR2 scheme is used for the treatment of viscous terms, with the  $\eta_{BR2}$  penalty parameter set to the number of faces of the cell. The meshes used in this section are the same meshes which were used in the previous section, such that the results are comparable.

#### 5.3.1. Hexahedral meshes

The different rDG methods are first tested on regular and randomly perturbed hexahedral meshes. For this, the RANS-SAneg equations are solved. Even though the RANS-SAneg equations not only introduce viscous effects but also source terms, all differences in the error behaviour are related to the viscous fluxes, as the MMS also includes source terms in the Euler equations. The results for the hexahedral meshes can be seen in figure 5.6.

From the figure, it can be seen that all methods reach their designed order of accuracy. The rDG methods reach slightly higher orders of accuracy than 3. In contrast to previous results, the least-squares rDG method results in a higher magnitude of error compared to the native DG method for a comparable number of degrees of freedom. Furthermore, variational reconstruction does not perform as well as the higher-order DG method on the same mesh, as was seen for the Euler equations. However, it still performs better than a native DG method per degree of freedom. As for the Euler equations, the extended least-squares method leads to a higher

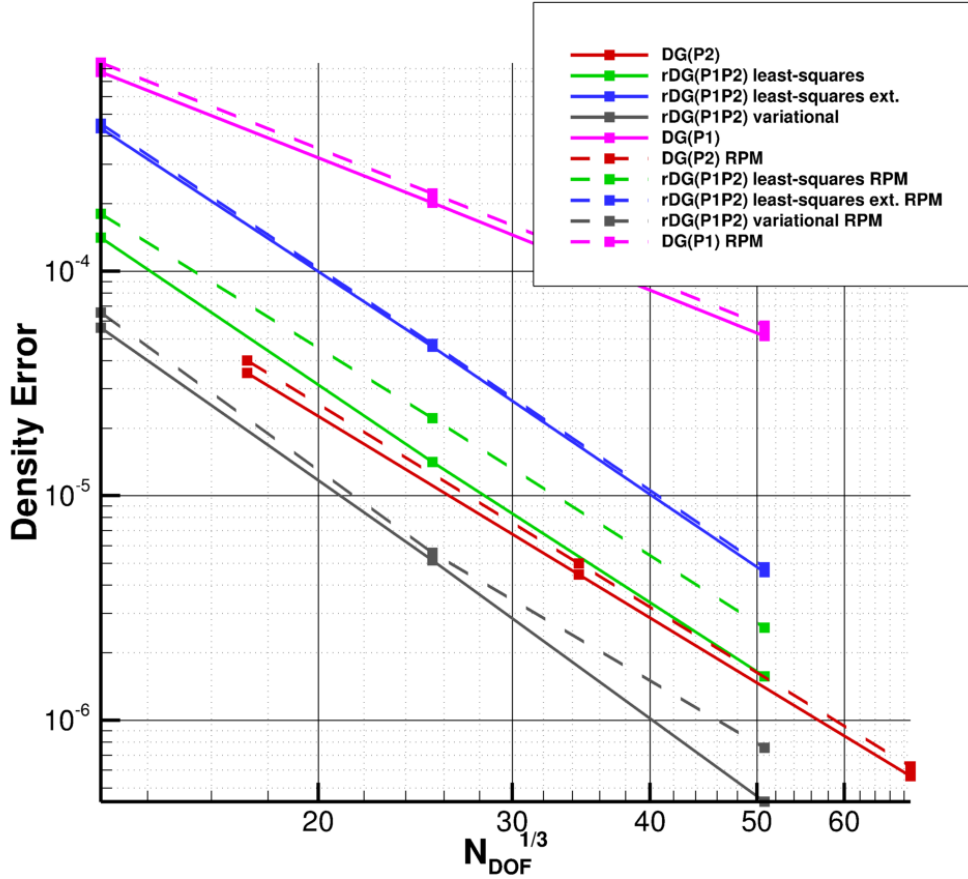


Figure 5.6: Density Error against cube root of the number of degrees of freedom on a regular hexahedral grid and a randomly perturbed hexahedral mesh for the RANS-SA-negative equations.

absolute error than the standard least-squares method; it is, however, less sensitive to a randomly perturbed mesh than the other rDG methods, as well as the native DG method.

### 5.3.2. Tetrahedral mesh

The results for the rDG methods on tetrahedral meshes can be seen in figure 5.7. It can be seen that both the extended least-squares and the variational reconstruction reach their designed order of accuracy. The standard least-squares rDG method is not present, as it is not stable on simplicial meshes, as noted before in section 5.2. As in the results for the hexahedral meshes, the least squares reconstruction performs worse than the native DG method of comparable order for an equivalent number of degrees of freedom. The variational reconstruction performs better than the DG method per degree of freedom. It cannot, however, reproduce the same improvement as can be observed for the Euler equations.

This deterioration in the performance of the rDG methods for viscous flows indicates a problem in the viscous treatment for the rDG methods. This will be investigated in the following section.

## 5.4. Viscous treatment in rDG methods

As seen in the previous section, the rDG methods perform worse for viscous flows compared to their performance for inviscid flows. The cause of this change in behaviour will be investigated in this section. It will first be investigated whether the behaviour is only present for the BR2 scheme used previously, or also for the BR1 scheme. Furthermore, as the BR2 scheme contains a user tunable parameter, its influence on the scheme will be investigated. Finally, the difference in linear stability between native and reconstructed DG methods for pure diffusion problems will be investigated numerically.

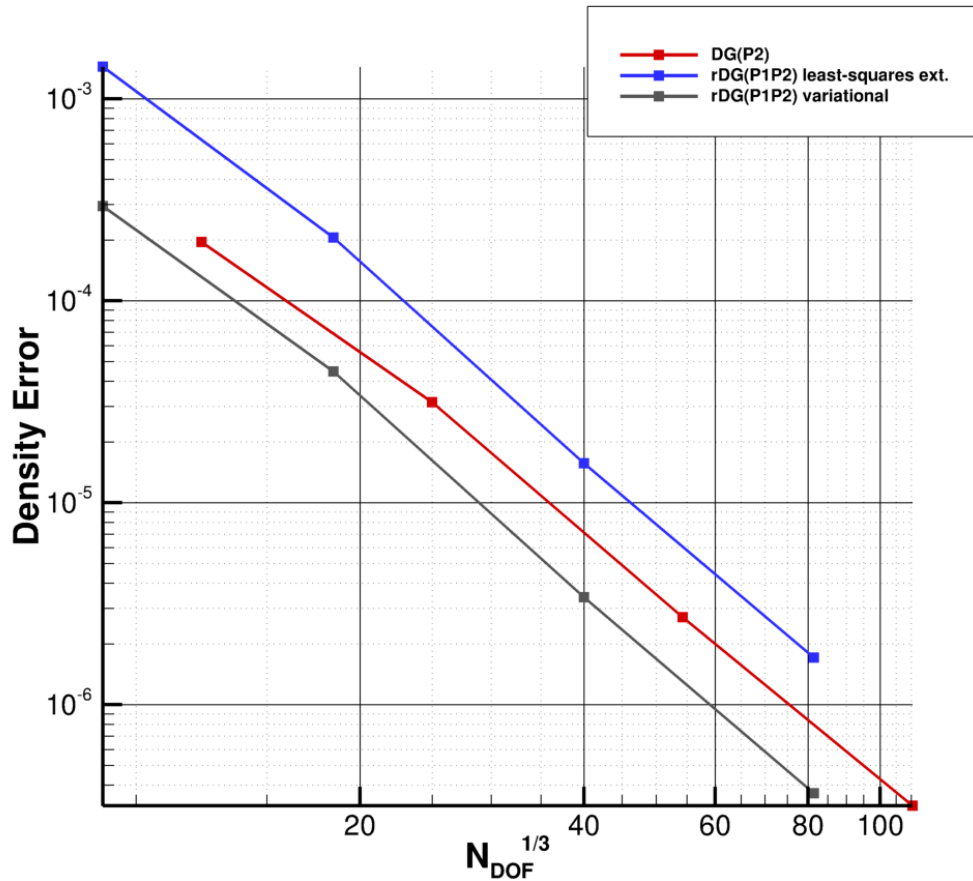


Figure 5.7: Density Error against cube root of the number of degrees of freedom on a tetrahedral mesh for the RANS-SA-negative equations.

#### 5.4.1. BR1 vs BR2 scheme

Two different viscous schemes are considered for the DG and rDG methods. These schemes are the BR1 scheme [5] and the BR2 scheme [9]. A comparison between the BR1 and BR2 schemes can be seen in figure 5.8. For the native DG method, the difference between the BR2 and BR1 schemes is very small. For the rDG methods, however, a strong difference can be seen between the two treatments. The BR1 scheme significantly decreases the error of the least-squares rDG method on coarse grids. The difference between both schemes decreases when the mesh gets refined. Similar observations can be made for the variational reconstruction; however, the decrease in error is less. When comparing the behaviour of the BR1 scheme to the MMS for the Euler equations (fig. 5.1), it can be seen that the good behaviour seen for pure convective problems is recovered.

#### 5.4.2. Influence of the penalty parameter $\eta$

As the BR2 scheme, in its implemented form [11] features a user-tunable parameter  $\eta$ , its influence will be investigated. The choice recommended for  $\eta$  by Brezzi et al. [11] is to use the number of faces of the cell of interest. It is known that as the  $\eta$  increases, the viscous scheme becomes more diffusive. Thus, a second option with  $\eta = 2$  will be investigated. This choice results from the observation that  $\eta$  emulates the influence of the missing faces in the local lifting. However, only faces with a normal vector  $\mathbf{n} \cdot \mathbf{n}_i \neq 0$ , where  $\mathbf{n}_i$  is the normal vector of the face of interest, are relevant. For a regular hexahedron, this results in a value of 2 for  $\eta$ . It should be noted, that this value for  $\eta$  is only justifiable for sufficiently regular hexahedrons, and higher values might be necessary for highly skewed elements. The results of the parameter study can be seen in figure 5.9.

It can be seen that reducing the value of  $\eta$ , reduces the error for both the rDG and the DG methods. The magnitude of change for the DG method is significantly smaller than for the rDG method. For a value of  $\eta = 2$ ,

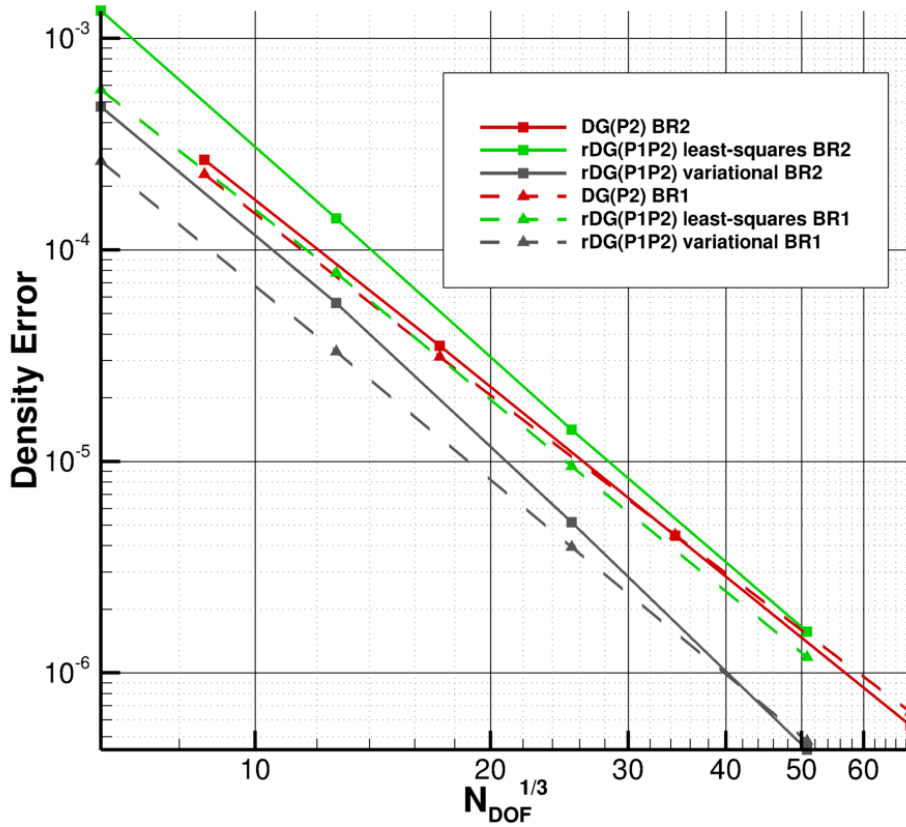


Figure 5.8: Comparison of the density for the BR1 and BR2 scheme on a regular hexahedral grid for DG and rDG methods.

the difference between the rDG and DG methods almost vanishes. Furthermore, the influence of  $\eta$  appears to diminish on very fine meshes.

### 5.4.3. Stability of viscous fluxes

The strong sensitivity to  $\eta$  in the case of rDG methods, as well as the stark difference in behaviour between DG and rDG methods, suggests significant changes in the eigenvalues of discretization, leading to a difference in linear stability for rDG methods compared to the underlying DG methods. Dumbser et al. [19], showed that for pure convective problems, the von Neumann stability of rDG methods is solely determined by the underlying DG method. To investigate, if this still holds for pure diffusive problems, using the BR2 scheme, the following one-dimensional scalar PDE is used.

$$\mu \frac{\partial^2 u}{\partial x^2} = \frac{\partial u}{\partial t} \quad (5.4)$$

The equation is discretized using a least-squares rDG method, as well as a native DG method. For both methods, the stability margin is calculated approximately using two different approaches.

**Approximate eigenvalue analysis** The first approach is based on a numerical approach by Hickel et al. [26]. In this approach, the eigenfunctions of the discretization are assumed to be of the form  $u = e^{ikx}$ . This is valid for a discretization with a circulant matrix, such as finite volume methods. For DG methods, the matrix itself is not circulant as each cell consists of several degrees of freedom, resulting in a block circulant matrix. The assumed eigenmodes are then propagated through the discretization to determine their corresponding eigenvalues. A comparison between the exact and assumed eigenmodes is presented in figure 5.10 of a DG(P1) method for the linear advection equation.

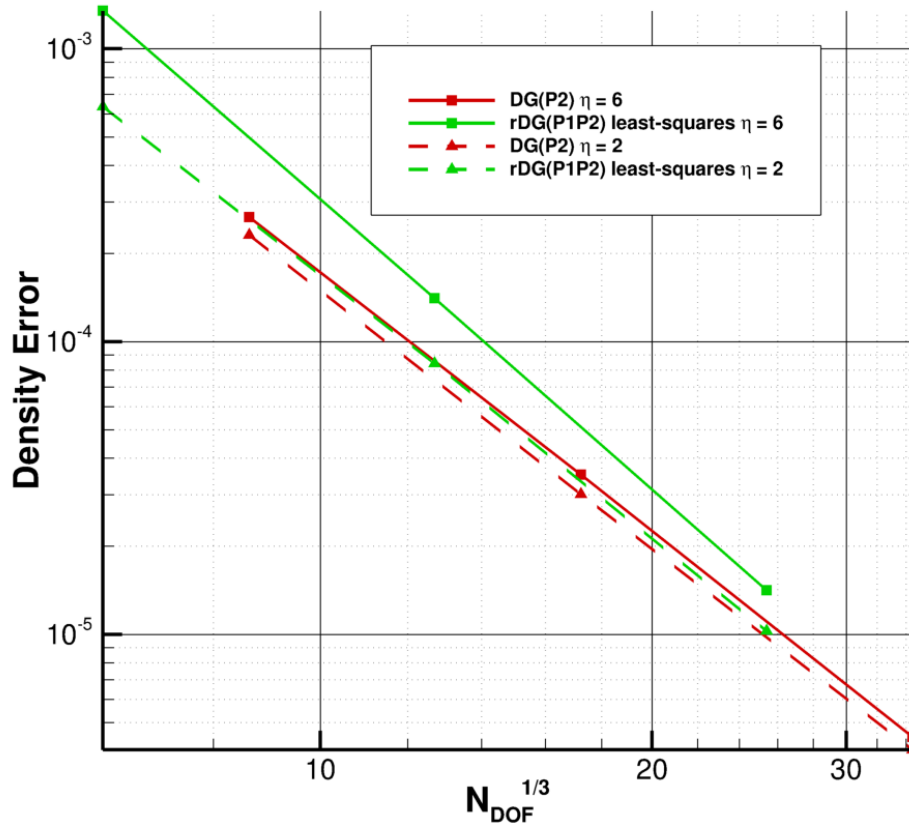


Figure 5.9: Influence of the  $\eta$  parameter in the BR2 scheme on the Density Error on a hexahedral grid.

From the figure it can be seen that for the lowest eigenmode, both the analytical and the assumed eigenvector match very well. When however moving to higher frequency eigenmodes, the discrepancy between analytical and assumed eigenmodes grows. Thus, it can be assumed that the assumed sine waves are a good approximation for the low-frequency eigenmodes. As the high-frequency eigenmodes are affected the most, however, the stability limit obtained by this method may be affected significantly.

**Maximum eigenvalue analysis** A second approach is based on using the stability limit of the forward Euler (FE) time-stepping method, to estimate the maximum eigenvalue of the solution. For this approach, it is assumed that  $|\mathcal{R}(\lambda_i)| \gg |\mathcal{I}(\lambda_i)|$  and  $\mathcal{R}(\lambda_i) \leq 0$  for  $i = 0, 1, 2, \dots$ . A diffusive CFL number (DCFL) is then defined as  $DCFL = \frac{dt}{\mu dx^2}$ . The value of the DCFL, where a FE method diverges, can then be found using a bisection search. From the result, of this bisection search, the maximum eigenvalue of the method can then be calculated as  $\lambda_{\max} = -2/DCFL$ .

To make sure, this numerical approach yields the correct approach, a suitable initial condition needs to be chosen, such that all eigenmodes of the discretization are excited. For a circulant matrix, it is known that the eigenmodes are of the form  $u = e^{ikx}$ . Thus, a suitable initial condition should excite all representable Fourier modes. For the initial condition  $u_0 = e^{-x^2}$ , which satisfies this requirement is chosen. The two approaches were verified for an FV scheme, for which the maximum eigenvalue is known analytically. The results of the verification can be seen in

The methods were then applied to different rDG and DG discretizations. For the rDG methods, a no-op reconstruction was chosen, such that all additional degrees of freedom were kept to zero, to isolate the influence of the viscous BR2 treatment on the eigenvalues. The results can be seen in figure 5.11.

Comparing the rDG(P0P1) in figure 5.11b to its underlying DG method, it can be seen that the rDG method has a nearly 4 times higher eigenvalue than the underlying method. This is due to the presence of first-

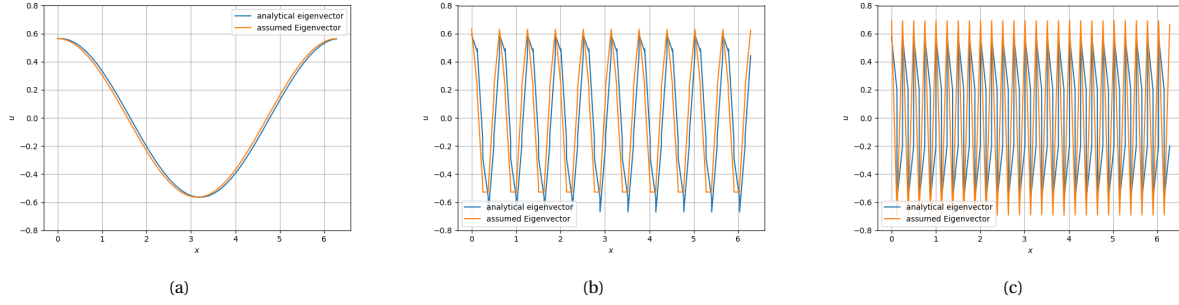


Figure 5.10: (a) Comparison between the analytical and assumed first non-constant eigenmode. (b) Comparison between the 10<sup>th</sup> analytical and assumed eigenmodes. (c) Comparison between the highest analytical and assumed eigenmodes

Table 5.2: Verification of the numerical methods for estimating the maximum eigenvalue of the discretization

	$\lambda_{\max}$	Error%
Analytical	-4	-
Approximate Eigenvalue	-3.996	0.1
Numerical stability	-3.9214	1.965

order polynomials in the expression of the lifting operator. These higher-order contributions to the lifting operator increase the eigenvalues of the discretization. However, it can also be seen that the eigenvalues of the rDG(P0P1) method are lower than for a DG method of comparable order. This indicates that the influence of higher-order lifting contributions for rDG methods is not as high as for native DG methods, for a constant reconstruction rDG method. Similar observations can be made for an rDG(P1P2) method, as can be seen in figure 5.11a. It is, however, unclear if the decrease in stability will lead to noticeably different stability limitations for more complex test cases.

#### 5.4.4. Further treatment of viscous terms

This section has presented the difference between the expected behaviour for the BR2 scheme in rDG methods and the observed behaviour. It furthermore presented changes to the numerical method which can recover the expected behaviour or at least reduce discrepancies significantly. It was shown that the BR1 scheme can recover the expected error behaviour of rDG methods for viscous flows. For the BR2 scheme itself, it was shown that a  $\eta$  of 2 can significantly improve the error constant of the rDG methods compared to the standard value of  $\eta$ , however, this change does not completely recover the expected behaviour of the rDG methods. In further chapters, the BR2 scheme will be used nonetheless, with a value of 2 for  $\eta$ . This choice is motivated by the fact, that the BR2 scheme provides significantly improved stability compared to the BR1 scheme, as the computation of fluxes in the BR1 scheme involves second-order neighbours [10], leading to stiffer numerical systems. Furthermore, the BR2 scheme is fully differentiated in the code used, while the BR1 scheme is not, leading to improved preconditioning for cases using the BR2 scheme compared to those using the BR1 scheme.

## 5.5. Conclusion

It was shown that rDG methods can reach the expected order of accuracy for viscous and inviscid flows on hexahedral and tetrahedral meshes. Furthermore, the effect of nonplanar faces has been demonstrated on randomly perturbed hexahedral meshes. The extended stencil did not show a significant increase in absolute error due to this disturbance, while the least-squares reconstructions and variational reconstructions showed an increase in absolute error while retaining their designed order of accuracy. In general, however, the extended stencil least-squares performed worse than the standard least-squares and variational reconstructions on hexahedral grids, while being necessary for the convergence of least-squares reconstruction methods on tetrahedral grids. Contrary to previous observations by Cheng et al. [13], it was found that variational reconstruction performs significantly better than both a least-squares reconstruction method and a native DG method in terms of error per degree of freedom. From the formulation of variational reconstruction, it can be seen that the reconstruction problem is a global problem, which imposes continuity of all represented derivatives over the domain. As the manufactured solution is smooth over all derivatives by definition, it is

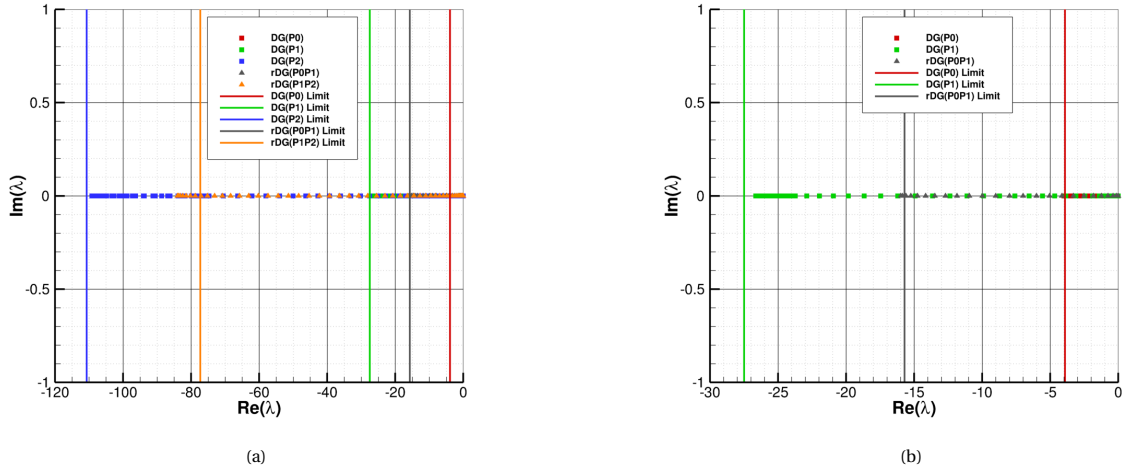


Figure 5.11: (a) Approximate Eigenvalues and Numerical Stability Limits for rDG and DG Methods up to third order. (b) Approximate eigenvalues and numerical stability limits for rDG and DG methods up to second order.

to be expected that a variational reconstruction performs very well. Contrary to that, a least-squares reconstruction aims to reconstruct the underlying solution of neighbouring cells, while the reconstructed degrees of freedom on the cell are ignored.

For viscous flows, there is a deterioration in absolute error compared to inviscid flows. It was shown that this discrepancy can be fully eliminated by using the BR1 scheme instead of the BR2 scheme. Furthermore, a decrease in the value of  $\eta$  reduces the absolute error of the BR2 scheme and therefore can reduce the discrepancy. The stability margins previously noted by Dumbser et al. [19] for hyperbolic problems were shown to not be valid for viscous flows treated with the BR2 scheme. It was shown that the maximum eigenvalue for rDG methods is larger than the one of the underlying DG method, but lower than the maximum value of a DG of comparable order. As only the maximum eigenvalue is affected, the condition number of the matrix increases, leading to a stiffer numerical problem.

# 6

## Results

In the previous chapter, it was shown that the numerical methods are implemented correctly and produce the expected order of accuracy. However, the cases considered up to now are not representative of problems in which RANS simulations are usually used. This chapter aims to move from simple inviscid flow cases in two dimensions to complex two-dimensional and three-dimensional flows.

First general settings for the computations are laid out in section 6.1. Sections 6.2 - 6.6 will then present different test cases in two dimensions. Finally, section 6.7 will examine rDG methods on a three-dimensional RANS test case.

### 6.1. General settings

For the inviscid flow test cases, the Jacobian of the underlying DG method is used as an approximation for the Jacobian of the rDG methods. This approximation leads to divergence for the considered viscous test cases. Thus, the exact directional derivative is calculated using automatic differentiation. As the rDG methods are compared to a DG method of comparable order, the computational time is compared for the computation starting from a converged DG(P1) solution.

### 6.2. Smooth bump

The smooth bump case considers an inviscid flow through a channel that is disturbed by an Eulerian bump. The Mach number of the flow is 0.5. At the inlet, a total pressure and total temperature are imposed, while at the outflow, a static pressure boundary condition is imposed. The top and bottom walls are treated as slip wall boundary conditions.

This test case is used to evaluate the performance of rDG methods for hyperbolic problems. To judge the error of the solution, the integrated entropy error is recorded for every mesh.

$$S_{err} = \sqrt{\frac{\int_{\Omega} \left( \frac{s-s_{\infty}}{s_{\infty}} \right)^2 dV}{\int_{\Omega} dV}} \quad (6.1)$$

This test case is also used to evaluate the effect of the partial solving of the variational reconstruction problem as discussed in section 3.3.2. The mesh as well as an exemplary Mach number distribution can be seen in figure 6.1. The solution was considered converged if the freestream residual was reduced by 10 orders of magnitude. The results can be seen in figure 6.2.

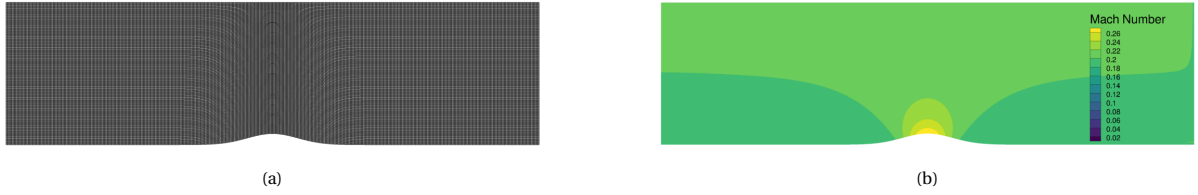


Figure 6.1: (a) Finest mesh of the mesh cascade used for the smooth bump test case. (b) Mach Number distribution for the smooth bump test case.

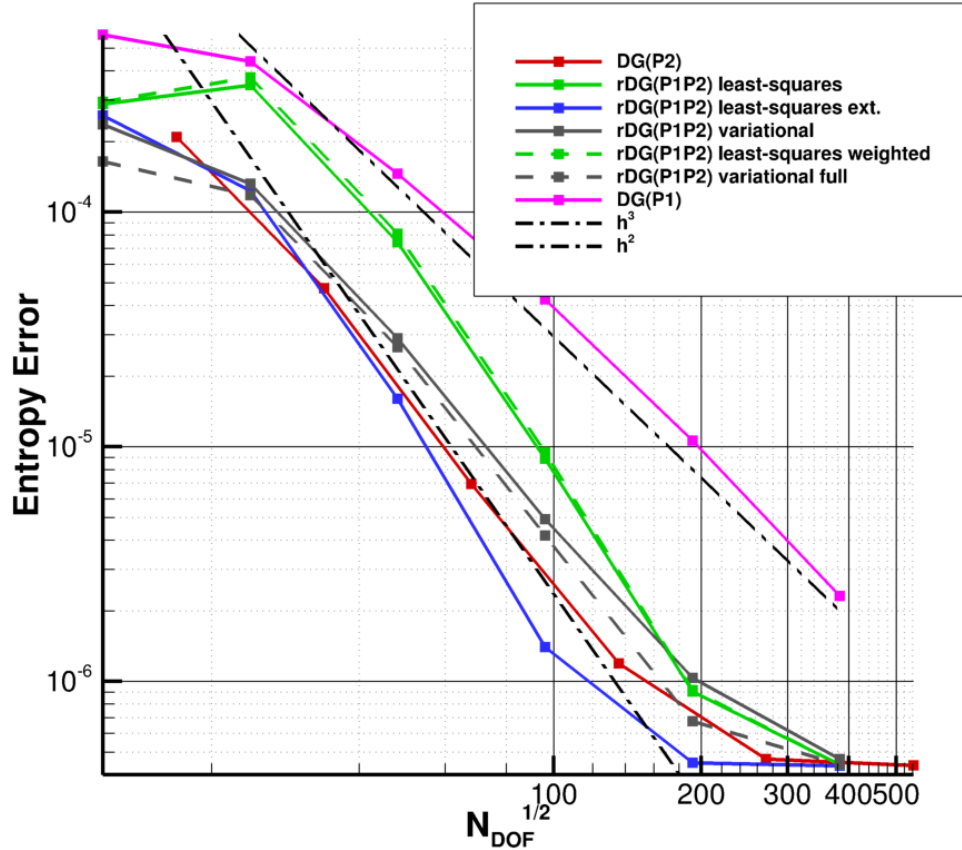


Figure 6.2: Integrated entropy error of different rDG methods against the number of degrees of freedom for the smooth bump test case.

It can be seen that all considered methods reach their designed order of convergence as indicated by the black lines. The weighting inside the least-squares method does not show a significant influence on the results, which is to be expected, as the mesh is mostly isotropic. Furthermore, it can be seen that the variational reconstruction performs better than the least-squares reconstruction.

For the variational reconstruction, two different solution approaches are evaluated. In the dashed line, the linear reconstruction problem is solved completely at every iteration, while for the continuous line, the linear system is only solved approximately with two symmetric Gauss-Seidel sweeps at every iteration, starting from a zero vector. Even though this approach is not formally third order, it can be seen that the results still perform better than a least-squares reconstruction. The increase in error of the approximate variational reconstruction grows for refined meshes, which is to be expected, as the Gauss-Seidel sweeps involve a lower fraction of the mesh in the reconstruction for larger meshes.

A further method that is evaluated is the extended least-squares method. In contrast to the previously considered three-dimensional manufactured solution cases, in two dimensions on a hexahedral grid, the

additional link contributions only add 4 more elements to the stencil, as can be seen in figure 6.3, which are weighted lower than the original elements due to their further distance from the original cell. The extended least-squares method in blue performs very well in two dimensions for the test case and can recover the behaviour of the native DG method for the finest three meshes.



Figure 6.3: (a) Compact face-based stencil on the example of a structured quadrilateral mesh. (b) Extended node-based stencil on the example of a quadrilateral triangular mesh.

### 6.3. Zero pressure gradient flat plate

The second test case is used to evaluate the influence of the introduced inverse distance weighting for highly anisotropic meshes. For this the zero pressure gradient flat plate (2DZP) from the NASA turbulence modelling resource<sup>1</sup> is used. The mesh used for the test case can be seen in figure 6.4. The flow enters the domain at a Mach number of 0.2, through an inlet boundary condition with fixed total pressure and total temperature. The flow leaves the domain at a constant static pressure. A Riemann farfield condition is imposed on the upper end of the domain, and a no-slip adiabatic wall is imposed on the flat plate itself. The first cell, even for the coarsest mesh, has a  $y^+$  value of 1.42 and is thus well resolved enough for all higher-order methods. To determine the convergence of the nonlinear solution process, a residual reduction threshold of  $10^{-10}$  is used compared to the freestream residual. The CFL number for the third-order DG method had to be half the CFL number used for rDG methods, to ensure the stability of the convergence process. Furthermore, all third-order simulations were initialised from a second-order native DG method, to speed up the computation and reflect best practices in the application of higher-order DG methods.

To judge the error of the solution, a reference value for  $C_D$  is computed, by an extrapolation of the results from the DG(P2) method. For this, the numerical apparent order is calculated to be 1.5 using the procedure proposed by Celik et al. [12], which is then used to do a Richardson extrapolation to the next finest grid level. It should be noted, that the numerical order obtained for the flat plate is not expected to match the designed order of accuracy, as the case features a singularity at the leading edge of the flat plate. The procedure for the DG(P2) method can be seen in table 6.1. The difference between this extrapolated reference value and the computed values for  $C_D$  can be seen in figure 6.5a.

Table 6.1: Drag Coefficients of the three finest grids for a DG(P2) method with the extrapolated value using the procedure by Celik et al. [12]

	Mesh Size	$C_D$	$\Delta C_D$
Measured	$69 \times 49$	$2.860268 \times 10^{-3}$	
	$137 \times 97$	$2.859416 \times 10^{-3}$	$8.519851 \times 10^{-7}$
	$273 \times 133$	$2.859115 \times 10^{-3}$	$3.014969 \times 10^{-7}$
Extrapolated	$545 \times 385$	$2.858950 \times 10^{-3}$	$1.651268 \times 10^{-7}$

The unweighted least-squares method can be seen to perform comparably to the higher-order DG method on the two medium meshes while displaying a lower error on the finest mesh. In contrast the weighted standard least-squares and weighted extended least-squares perform better on the two medium meshes than both the compact-stencil least-squares and the native DG(P2) method. This indicates that the introduced weighting parameter helps to improve the reconstruction in regions of high anisotropy. Furthermore, it can

<sup>1</sup><https://turbmodels.larc.nasa.gov/flatplate.html>

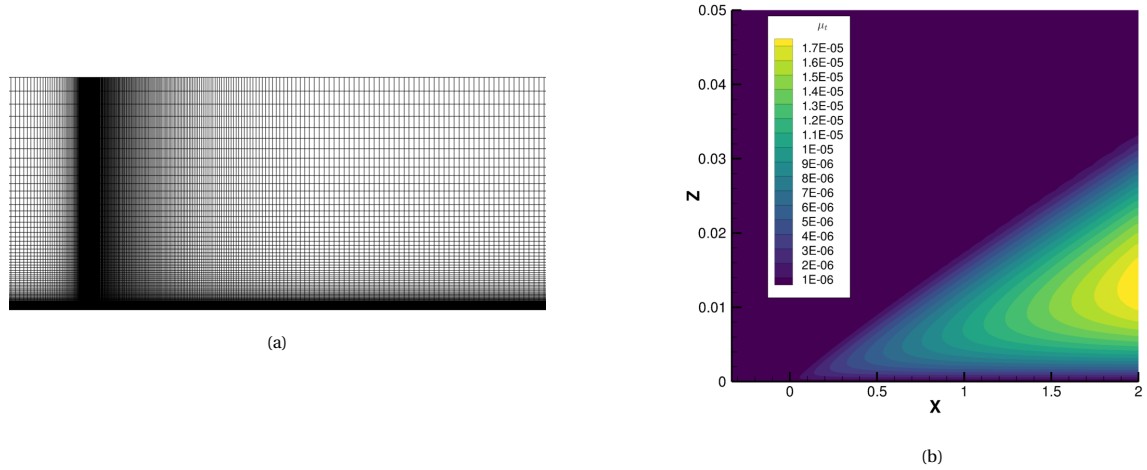


Figure 6.4: (a) Finest mesh in the mesh cascade for the flat plate test case from the NASA turbulence modelling resource. (b) Distribution of the transported turbulent variable close to the leading edge of the plate for the flat plate test case.

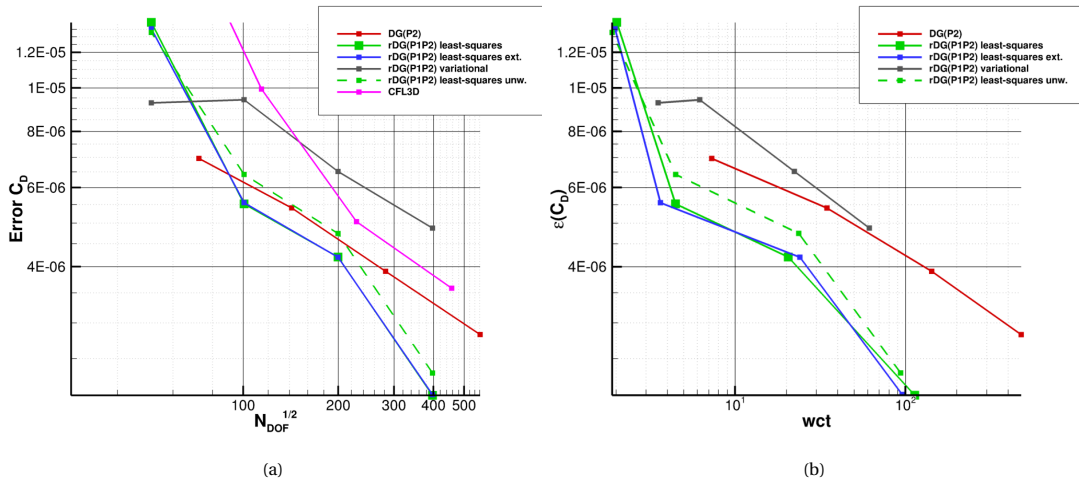


Figure 6.5: (a) Error of  $C_D$  against the number of degrees of freedom per dimension for different discontinuous Galerkin and reconstructed discontinuous Galerkin methods.

be seen that the extension of the stencil in the least squares method does not affect the value of  $C_D$  significantly. This is to be expected, as all additional elements included in the stencil are further away than the original elements in the stencil and thus their influence is low compared to the original stencil elements. Both the least-squares methods and the native DG(P2) methods perform better than the second-order finite volume code CFL3D, for which reference results are available.

On the other hand, the variational reconstruction seems to perform worse than all other considered methods for a given number of degrees of freedom. For each simulation the run time is recorded, for which the results can be seen in figure 6.5b.

From the figure, it can be seen that the rDG methods provide a significant improvement in wall clock time for a given level of error. It furthermore can be observed, that the introduction of an inverse distance weighting does not significantly affect the run time of the rDG method. When comparing the weighted least-squares with its extended version, it can be seen that the inclusion of additional stencil elements does not negatively affect the run time for this test case. This, however, might not translate to other test cases, as the influence of the additional elements is very low compared to the original stencil elements for large regions of the mesh. Again visible is the increased error of the variational reconstruction, compared to that of the native DG method and the least-squares rDG methods.

To investigate this unexpected behaviour of the variational reconstruction, the solution on the finest mesh is analysed. As the variational reconstruction is global in nature, as even 2 symmetric Gauss-Seidel sweeps include fourth-order neighbours in the reconstruction, the singularity at the flat plate leading edge and its corresponding discontinuity are suspected to affect the variational reconstruction. For this, the results of a DG(P1) and different rDG methods are compared to the solution of a DG(P2) on the same mesh. The error  $\epsilon$  for each cell reported is calculated as

$$\epsilon = \frac{\sqrt{\int_{\Omega} (\mathbf{u} - \mathbf{u}_{ref})^2 d\Omega}}{V} \quad (6.2)$$

where  $V$  is the volume of the cell. The distribution of the Density error in the first cell of the boundary layer can be seen in figure 6.6.

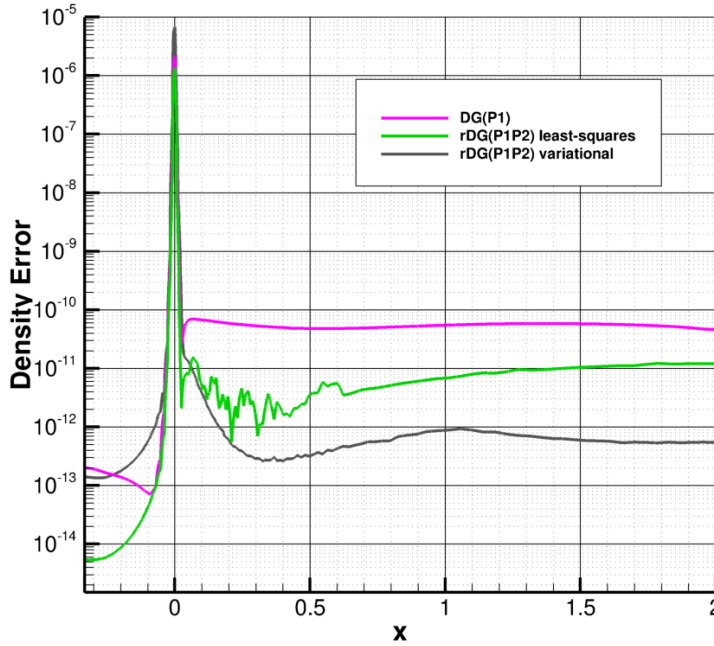


Figure 6.6: Density error of rDG(P1P2) and DG(P1) methods against a DG(P2) solution for the flat plate test case on the finest mesh.

The flat plate starts at  $x = 0$ , where all methods exhibit the biggest error against the DG(P2) method. It can be seen that the variational method offers the lowest error on the flat plate, which is in line with previous observations from the method of manufactured solutions and the smooth bump test case. The weighted least-squares method features a lower error than the DG(P1) method but a larger error than the variational reconstruction. Around the singularity, the variational reconstruction has an error 10 times higher than the least-squares reconstruction method as well as the DG(P2) method. This confirms the problems of the variational reconstruction for singularities and explains the higher error of the variational reconstruction compared to the least-squares reconstruction for the flat plate test case.

From these results, it can be concluded that the inclusion of an inverse distance weighting can improve the quality of reconstruction for least-squares methods on highly anisotropic mesh regions. As such mesh regions occur in many CFD applications such as boundary layers, this inverse distance weighting will be used on all further applications in this work. Furthermore, it can be seen that variational reconstruction performs worse than the least-squares reconstruction on test cases which feature a singularity.

## 6.4. Low Reynolds number airfoil

To apply the implemented rDG methods to high Reynolds number flows, first the baseline for the performance of the implementation of the rDG methods for aerodynamic test cases needs to be established. For

this, a NACA0012 airfoil is simulated at a Reynolds number of 5000 and an angle of attack of  $1^\circ$  at a Mach number of 0.5. This Reynolds number falls in the range of previously computed cases for rDG methods and can thus serve as a comparison to different applications. Although a Reynolds number of 5000 does not necessitate the use of RANS from a physical modelling perspective, it serves to enable a comparison between the performance of high and low Reynolds number flows in the context of rDG methods. Compared to a higher Reynolds number flow, the boundary layer in this test case is bigger compared to the thickness of the airfoil. Furthermore, the cells in the boundary layer are more isotropic for this test case, as the wall-normal spacing for resolving the boundary layer can be larger.

One of the meshes used can be seen together with a computed solution in figure 6.7. Quadratic elements are used, as a linear boundary approximation will lead to a reduction in order and will introduce nonphysical expansion fans[6].

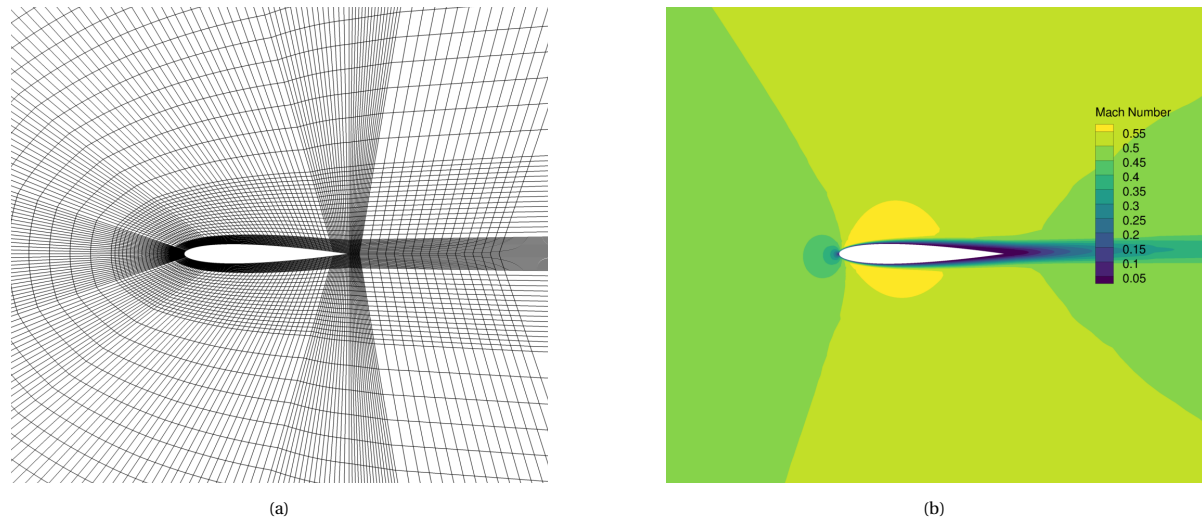


Figure 6.7: (a) Finest mesh of the mesh cascade used for the NACA0012 test case. (b) Mach number distribution of the converged third-order solution for the NACA0012 airfoil test case.

The far field is treated with a Riemann boundary condition, while the airfoil itself is treated with an adiabatic no-slip boundary condition. The solution was considered converged when the density residual was reduced by 10 orders of magnitude compared to the free-stream residual. The initial CFL number could be kept twice as high for the rDG methods compared to the DG method. Furthermore, all simulations have been started from a converged second-order DG method, to accelerate and stabilise the solution process. A reference value for the coefficient of drag was calculated using the previously discussed method by Celik et al. [12] from the three finest meshes of the DG(P2) method. The resulting errors for the coefficient of drag are shown in figure 6.8a. All least-squares rDG methods used an inverse weighting exponent of 1.0, to improve the solution in highly anisotropic regions of the mesh.

It can be seen that all rDG methods perform similar to a higher-order DG method in terms of degrees of freedom. The extended least-squares method performs worse than the standard least-squares method, especially on coarse meshes. This is in line with observations from the method of manufactured solutions and indicates that the extended stencil may involve elements which have an adverse effect on the quality of reconstruction. Variational reconstruction performs better than the other two rDG methods on the two medium meshes and can provide a significant improvement in terms of accuracy on the same mesh, however, the coarsest mesh did not converge using a variational reconstruction. The recorded run-times are reported in figure 6.8b.

In terms of wall clock time, the rDG methods perform better than the native DG methods for a comparable level of error. Similar to the previous results, the rDG methods converge significantly faster on the same mesh than a native DG method, which is expected due to the smaller size of the linear system in terms of block size. However it has more nonzero blocks overall and is thus denser. Due to the similar behaviour in error per degree of freedom, this translates to an overall improvement in wall clock time. The variational method, however, takes a longer time to converge than least-squares rDG methods.

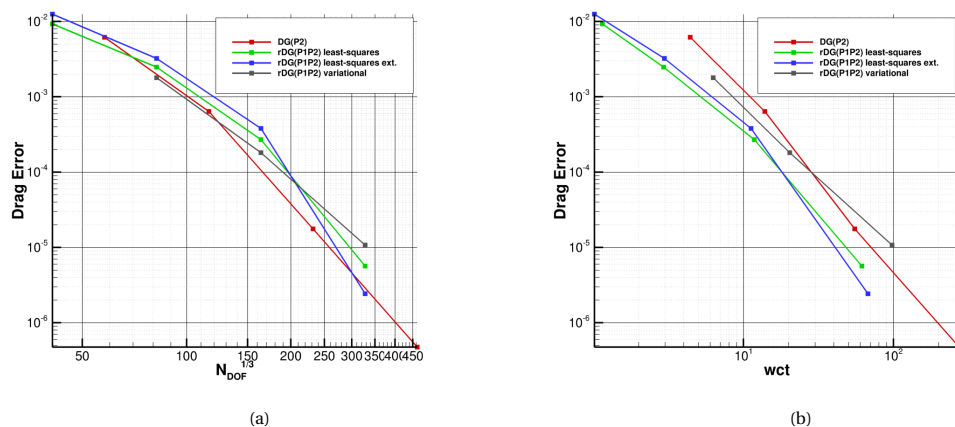


Figure 6.8: (a) Error of coefficient of drag against the number of degrees of freedom for the NACA0012 airfoil. (b) Error of coefficient of drag against computational time for the NACA0012 airfoil.

## 6.5. High Reynolds number airfoil

We now consider the performance of rDG methods for higher Reynolds numbers. For this, the Juskowski airfoil from the Higher-order CFD workshop 5<sup>2</sup> is used. The mesh was generated for a Reynolds number of 5 million and consists of quadratic hexahedrons, which can be seen in figure 6.9. From the figure it can be seen, that the elements in the boundary layer region are skewed, which may result in problems for the least-squares based rDG method. The flow enters the domain at a Mach number of 0.5 and an angle of attack of  $1^\circ$ , so that

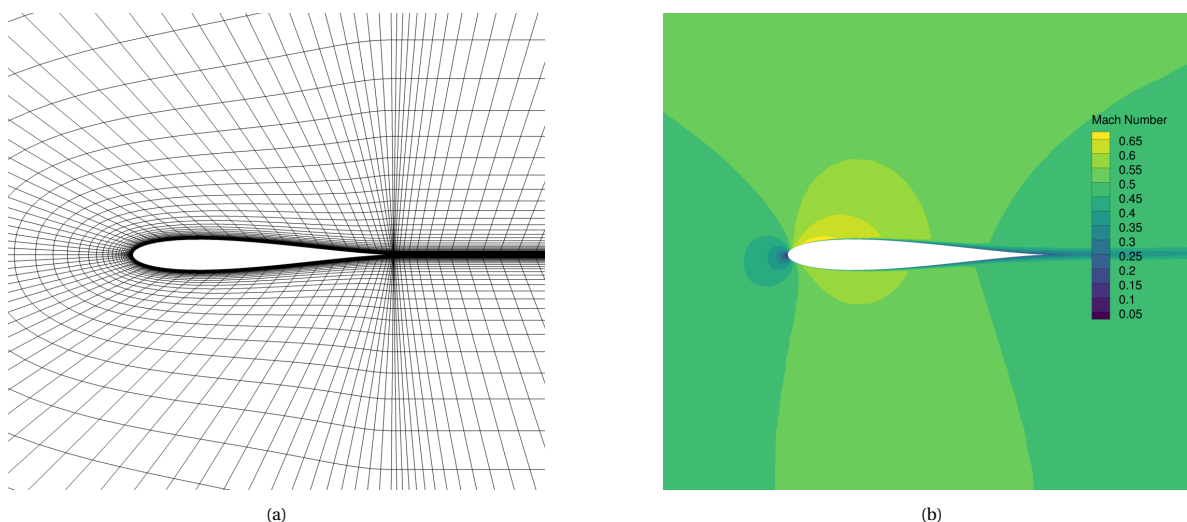


Figure 6.9: (a) Finest mesh of the mesh cascade used for the Juskowski airfoil test case. (b) Mach number distribution of the converged third-order solution for the Juskowski airfoil test case.

the simulation is comparable to the previous test case. The chord-based Reynolds number of the flow was set to  $5.7 \times 10^6$ . All meshes used in the simulation had a minimum  $y^+$  value of smaller than 1. The numerical settings and convergence criteria were kept the same as in the previous test case. The results obtained can be seen in figure 6.10. From figure 6.10a it can be seen, that the rDG methods perform significantly worse than the native third-order DG method in terms of error per degree of freedom. It should however be noted, that the coarsest mesh was not able to converge for the DG method. Variational reconstruction provides better results than least-squares reconstruction methods, this confirms the observations made in section 5.2.4, which suggest that skewed meshes do not negatively impact the discretization error for variational reconstruction based rDG methods. It was however, not able to converge on the finest mesh. In terms of

<sup>2</sup><https://how5.cenaero.be/>

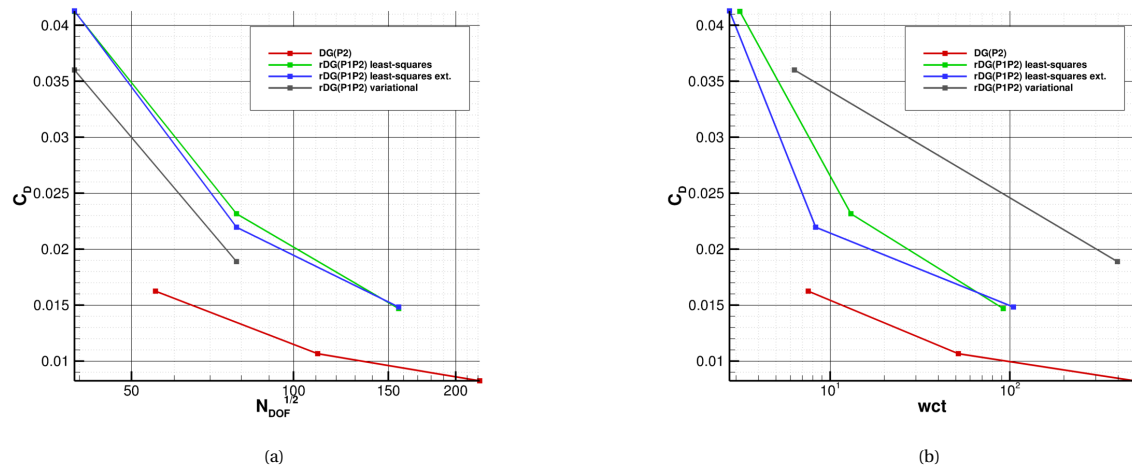


Figure 6.10: (a) Coefficient of drag against the number of degrees of freedom for a Juskowski airfoil. (b) Coefficient of drag against computational time for a Juskowski airfoil.

wall clock time, rDG methods do not offer any improvement over a higher-order DG method. Similar to the previous test case, the rDG methods converge faster on the same mesh. However, as the rDG methods perform significantly worse in terms of error per degree of freedom, this increase in computational speed does not lead to an overall better performance. This deterioration in error per degree of freedom might be influenced by significantly skewed elements in the airfoil boundary layer, which may adversely affect the quality of reconstruction. Such adverse effects on the reconstruction by skewed elements, are known from second-order finite volume methods.

## 6.6. Multi Element airfoil

This test case aims to evaluate the performance of rDG methods on more complex high Reynolds number flows. For this, the L1T2 high-lift airfoil was chosen. The freestream Mach number for this case is 0.2 with a Reynolds number of  $5.6 \times 10^6$  at an angle of attack of  $20.18^\circ$ . These flow conditions lead to a more complex flow structure than previous test cases, as can be seen in figure 6.11b. The meshes used for the test case were quadratic, however, the coarsest mesh used quartic elements, to ensure that no cells in the boundary layer encroach on each other. The integration degree for each mesh was chosen dependent on the order of the mesh. The medium fine mesh can be seen in figure 6.11a. The numerical settings and convergence criteria were the same as in previous test cases. For each mesh, the runtime and coefficients of drag and lift were recorded, which can be seen in figure 6.12.

In figure 6.12a, the drag and lift coefficients are compared to the number of degrees of freedom in the mesh. It should be noted that the finest mesh was not converged for the DG(P2) method due to prohibitively long computational times. Furthermore, the extended least-squares method was not able to be converged to the required tolerance for the finest considered mesh. As for the previous Juskowski airfoil, the rDG methods can not compete with the native DG method in terms of degrees of freedom. However, the variational reconstruction method performs the best of all considered rDG methods in terms of degrees of freedom. This is in line with the results obtained for the previous test case. When comparing the standard and extended least-squares methods to each other, it can be seen that the extended least-squares method produces slightly worse results compared to the standard least-squares method.

The comparison of convergence in terms of run-time can be seen in figure 6.12b. In this comparison, the rDG methods perform better than the native DG method. It can be seen that the variational rDG method takes the longest time to converge of all three methods. Furthermore, the extended least-squares method converges as fast as the standard least-squares method on all grids where it converges. It is notable, that the native DG method even on the finest grid can not compete with the rDG methods on a finer grid in terms of runtime. As both rDG and DG methods are initialised from a DG(P1) solution, the initial condition for the rDG method is closer to the converged solution compared to a higher-order DG method, which includes additional degrees of freedom. Furthermore, the linear system of the DG(P2) method was significantly more

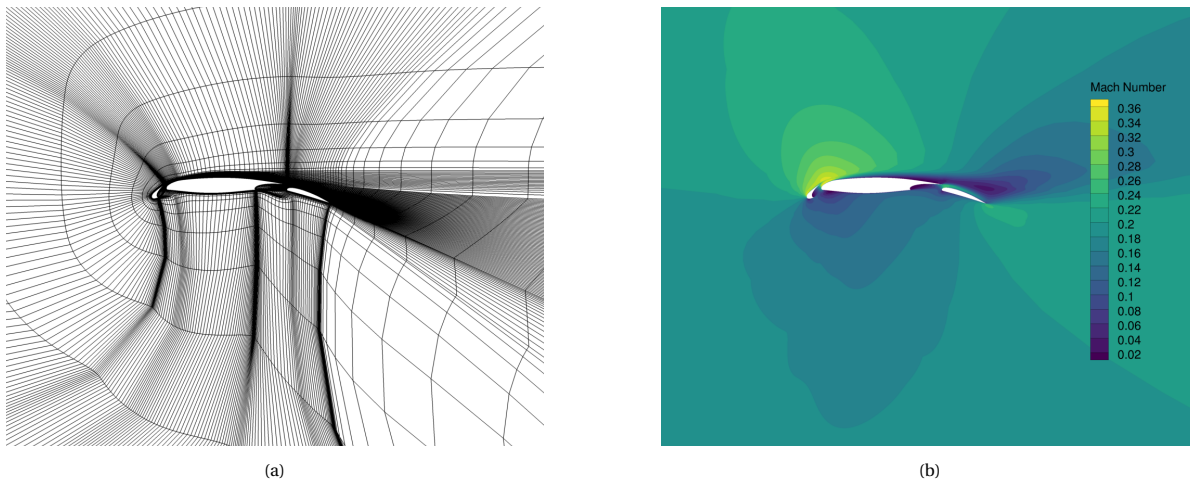


Figure 6.11: (a) Medium mesh for the LIT2 airfoil consisting of quadratic hexahedrons. (b) DG(P2) solution of the flow around the LIT2 airfoil on the medium mesh. The jagged flow field contours do not arise from numerical artefacts, but from the projection of the solution onto the elements as an element average.

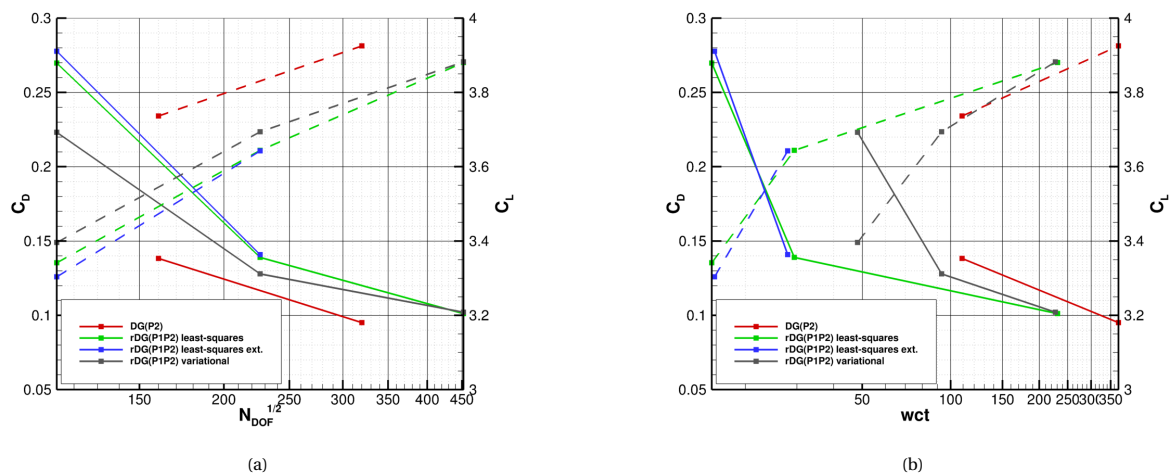


Figure 6.12: (a) Coefficient of drag in continuous lines and Coefficient of lift in dashed lines against the number of degrees of freedom for the LIT2 airfoil for different rDG and DG methods. (b) Coefficient of drag in continuous lines and Coefficient of lift in dashed lines against computational time for the LIT2 airfoil.

expensive to solve than the rDG methods leading to an increase in runtime. As the DG(P2) method takes a long time to converge, the rDG methods perform better than the native DG method in terms of lift and drag for a given runtime.

## 6.7. Hemisphere-cylinder

As a final test case, the Hemisphere-cylinder was selected. This case serves as a preliminary step for further three-dimensional simulations of aircraft configurations. The geometry and the surface mesh of the body and the symmetry plane can be seen in figure 6.13. The domain was meshed with quadratic hexahedrons and features a minimum  $y_+$  value of 1 or lower for every mesh. Special care in the creation of the mesh needed to be taken for the highly curved region at the front of the body. It was found that a low number of elements in this region leads to divergence in the case of rDG but not DG methods. This limitation in terms of mesh geometry is known from reconstruction-based finite volume methods.

The freestream Mach number of the test case is 0.6 at a diameter-based Reynolds number of  $3.5 \times 10^5$ , which translates to a Reynolds number of  $3.5 \times 10^6$  based on the length of the body. To not only replicate a simple boundary layer in three dimensions, but to also include more complex cross flow features, the body

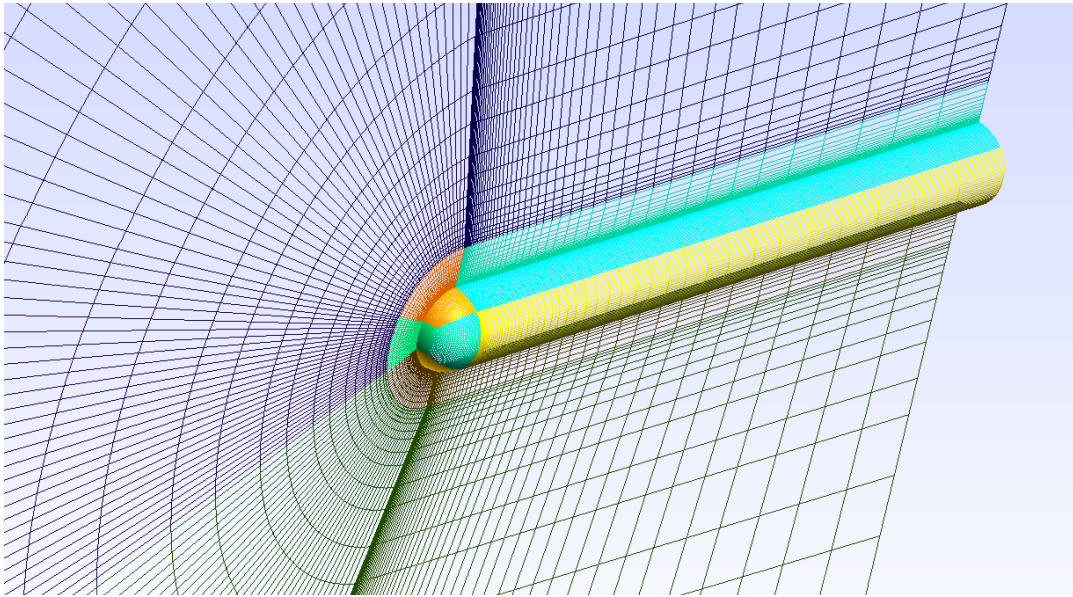


Figure 6.13: Finest hexahedral mesh for the Hemisphere-cylinder test case.

was also kept at an angle of attack of  $5^\circ$ . The numerical settings were kept from the previous test case; however, the convergence criteria were relaxed to a freestream residual reduction of  $10^{-8}$ . Results for the two meshes can be seen in figure 6.14.

It can be seen, that both considered rDG methods perform better than the underlying DG(P1) method. Furthermore, it can be seen that for this test case, the least-squares reconstruction method performs better than the variational method. This might be due to the approximate solving of the linear reconstruction problem, which is used to enable convergence. As even the coarsest mesh includes 54 thousand elements, the variational reconstruction only includes a small part of its required stencil. The least-squares method follows the higher-order DG solution well, even on the coarse mesh. The convergence histories both in terms of non-linear iterations and wall clock time can be seen in figure 6.15.

From figure 6.15a it can be seen that both rDG methods and native DG methods take approximately the same number of iterations to converge from a DG(P1) solution. Furthermore, it can be seen that the number of iterations taken with the third-order methods only represents a small fraction of the total number of iterations. In figure 6.15b, the density residual convergence is shown against the total computational time. It can be seen that the third-order DG method takes significantly more time to converge than the three reconstructed DG methods. This decrease in time per iteration leads to a lower computational time on the same mesh, which has been observed for all previous test cases. For the DG method, a stark reduction in convergence can be seen after around 180 seconds. This reduction in convergence results from the increased stiffness of the linear system due to the increase in CFL number.

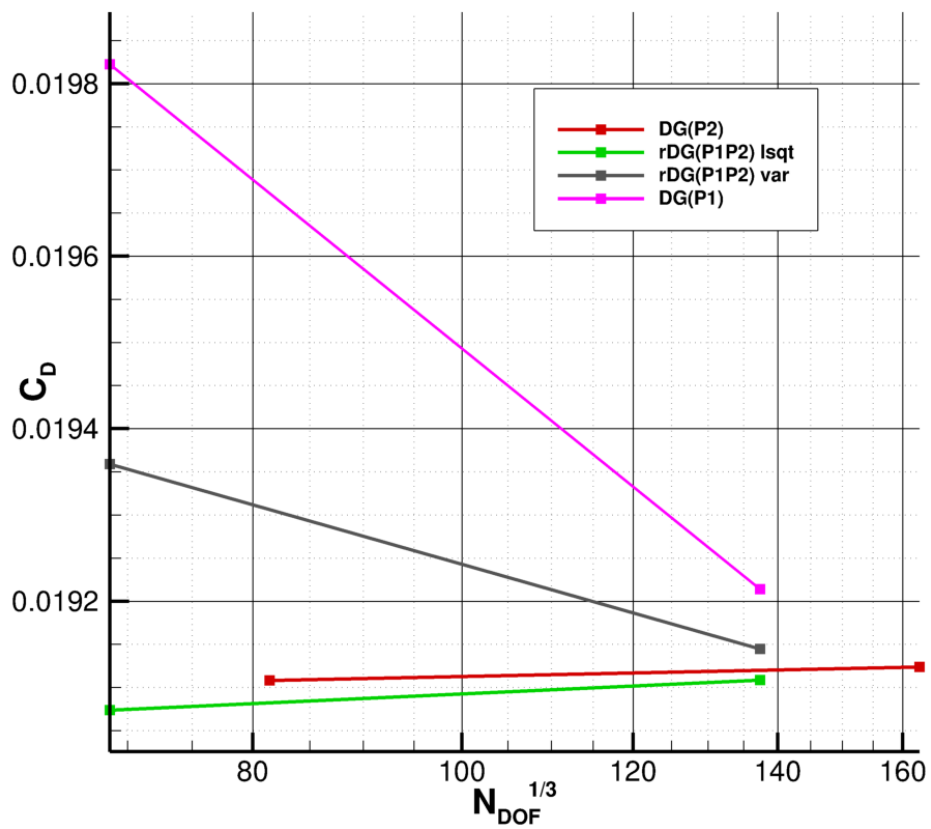


Figure 6.14: Coefficient of drag against the number of degrees of freedom for the Hemisphere-cylinder test case.

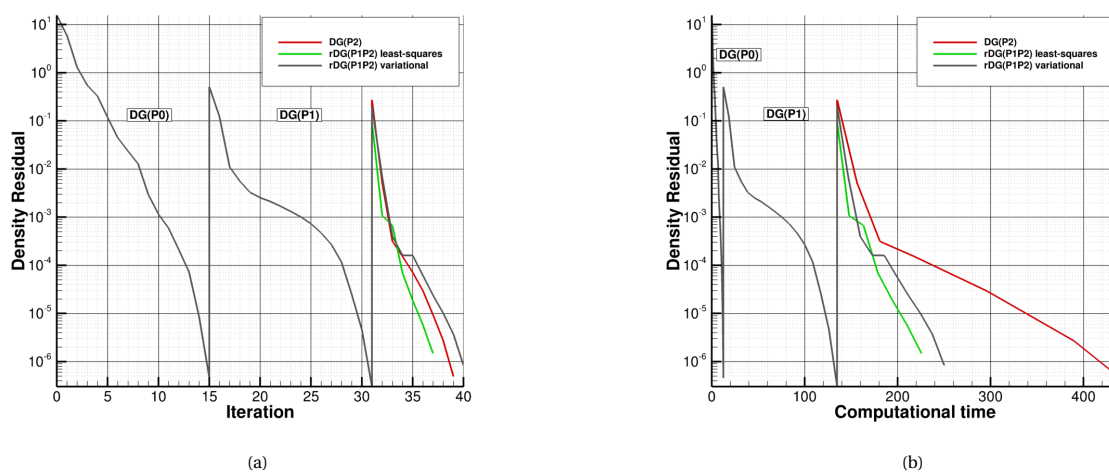


Figure 6.15: (a) Convergence of the density residual against the number of non-linear iterations for the Hemisphere-cylinder test-case. (b) Convergence of the density residual against total computational time for the Hemisphere-cylinder test case.



# 7

## Conclusion

In the previous two chapters, both implemented reconstruction methods were tested on several different cases. This chapter now aims to answer the research questions established in chapter 3.4. First, a general note about the spatial convergence of the rDG methods is given in section 7.1. Afterwards, sections 7.2 - 7.5 will answer the four research questions previously defined in section 3.4. Section 7.6, will summarise the performance of rDG in terms of mesh quality aspects. Finally, in section 7.7 recommendations for future work will be given.

### 7.1. Convergence of rDG methods

The designed order of accuracy of the least-squares based rDG (LS-rDG) methods and the variational rDG (VR-rDG) method has been confirmed using the method of manufactured solutions for the Euler and the RANS-SAneg equations on hexahedral and tetrahedral grids. Both methods have a performance which is at least comparable to that of a native DG method of equivalent order on both hexahedral and tetrahedral grids for purely hyperbolic problems. Contrary to previous observations by Cheng et al.[13], it was found that the VR-rDG method performs significantly better than a native DG method in terms of error per degree of freedom. The variational reconstruction can even match the accuracy of a higher-order DG method on the same mesh for the Euler equations. For the RANS-SAneg equations, a slight decrease in accuracy was observed for both rDG methods. However, the VR-rDG still performed better than a native DG method in terms of error per degree of freedom.

### 7.2. Influence of the viscous flux in rDG methods

This decrease in accuracy for viscous flows has been further examined using the method of manufactured solutions on a hexahedral grid for the RANS-SAneg equations. This degradation in accuracy was found to occur only when using the BR2 scheme, and a switch to the BR1 scheme recovered the observations made for purely hyperbolic problems. As the BR2 scheme includes a tunable parameter  $\eta$ , the influence of varying this parameter was evaluated. It was found that a decrease in  $\eta$  leads to higher accuracy for rDG methods. Furthermore, it was found that the influence of  $\eta$  on the discretization error of the solution is greater for the rDG methods than for native DG methods. However, due to the higher stability and easier convergence of the BR2 scheme compared to the BR1 scheme, the BR2 scheme was used for all further computations. Moreover, it was found that the viscous treatment in rDG methods increases the condition number of the discretization matrix. This increase in condition number results in a decreased stability margin for the linear diffusion equation compared to the underlying DG method.

### 7.3. Inverse distance weighting

In section 3.3.1 an inverse distance weighting was adopted from finite volume methods to the least-squares reconstruction in rDG methods. This modification aims to weigh the influence of the elements in the reconstruction stencil. For this, elements that are physically closer to the element for which the reconstruction is performed are weighted higher than elements farther away. This is helpful for anisotropic mesh regions, which are encountered in the boundary layer regions of RANS simulations. It was shown that this weighting

can increase the accuracy of least-squares reconstruction methods on meshes featuring highly anisotropic regions. For the zero pressure gradient flat plate, this inclusion of a weighting factor improved the least-squares reconstruction method, such that the error per degree of freedom was lower than for a native DG method of comparable order. The inverse distance weighting has been used for all two and three-dimensional RANS test cases.

#### 7.4. Applicability to high Reynolds number flows

Both reconstruction methods were compared to a native higher-order DG method in low and high Reynolds number test cases. For low Reynolds numbers ( $Re=5000$ ), it was found that rDG methods perform comparably in terms of error per degree of freedom to a higher-order DG method. Due to the lower cost of convergence, this leads to a lower error for a given computational time than a native DG method. For flows with higher Reynolds numbers, this advantage is diminished however and all tested rDG methods performed worse per degree of freedom than a comparable DG method. However, for very stiff numerical systems, it was found that rDG methods can provide an improvement in computational time compared to native DG methods. The stiffness of the numerical problem was assessed by the number of iterations needed to converge.

#### 7.5. Jacobian approximation

For the Euler equations, it was found that the Jacobian of the underlying DG method is sufficient to ensure the convergence of rDG methods. This approximation, however, is not sufficient for cases which include diffusive terms. For such cases, the exact Jacobian of the method needs to be calculated using either automatic differentiation or finite differences. The approximate Jacobian, however, is still sufficient as a preconditioner for the GMRES solver using the exact Jacobian. If however, more complex turbulence models than the considered Spalart-Allmaras model are used, the resulting increase in numerical stiffness may necessitate the use of an exact preconditioner.

#### 7.6. Influence of mesh quality

It was found, that the discretization error of the LS-rDG method increased on a mesh with randomly perturbed inner vertices, which lead to non-planar and skewed faces. This increase in discretization error was of similar magnitude as observed for the DG(P2) method. The extended stencil LS-rDG method proved more robust to the randomly perturbed mesh, and no significant increase in discretization error was observed for inviscid and viscous flows. The VR-rDG method exhibited a significant increase in discretization error on the randomly perturbed mesh. This was proven to be a result of the non-planar faces, as the variational reconstruction method showed no increase in discretization error on a skewed mesh with planar faces.

It was furthermore found that in regions of high surface curvature, the mesh needs to be sufficiently resolved to allow convergence of rDG methods. This is in contrast to native DG methods, which do not suffer from this restriction.

#### 7.7. Recommendations for future work

As rDG methods were found to be less robust than DG methods in terms of mesh resolution, an adaptive method may be needed, to combine rDG and DG methods for higher-order simulations. Such a combination may involve the use of DG methods in the boundary layer regions, which feature highly curved cells, and the use of rDG methods in regions further away from the body. Such a combination would decrease the number of degrees of freedom for a given mesh while retaining the formal order of accuracy and decreasing computational effort.

Furthermore, the reconstruction operators may be used in the p-staging startup process of higher-order DG methods, to gain a better initial state for the additional higher-order states. Such a higher-order prolongation may also be used in non-linear multigrid methods, to increase the rate of convergence, as has previously been explored by Hasselbacher [25] and Fallet [20] in the context of second-order finite volume methods.

# Bibliography

- [1] Mohammad Alhawwary and Z. J. Wang. “A Combined-Mode Fourier Analysis of DG Methods for Linear Parabolic Problems”. In: *SIAM Journal on Scientific Computing* 42.6 (Jan. 2020), A3825–A3858. ISSN: 1064-8275, 1095-7197. DOI: 10.1137/20M1316962. arXiv: 1810.03095.
- [2] Mohammad Alhawwary and Z. J. Wang. “Fourier Analysis and Evaluation of DG, FD and Compact Difference Methods for Conservation Laws”. In: *Journal of Computational Physics* 373 (Nov. 2018), pp. 835–862. ISSN: 00219991. DOI: 10.1016/j.jcp.2018.07.018. arXiv: 1802.02719.
- [3] Steven Allmaras, Forrester Johnson, and Philippe Spalart. “Modifications and clarifications for the implementation of the Spalart-Allmaras turbulence model”. In: *Seventh International Conference on Computational Fluid Dynamics (ICCFD7)* (Jan. 2012), pp. 1–11.
- [4] Douglas N. Arnold et al. “Unified Analysis of Discontinuous Galerkin Methods for Elliptic Problems”. In: *SIAM Journal on Numerical Analysis* 39.5 (2002), pp. 1749–1779. DOI: 10.1137/S0036142901384162. eprint: <https://doi.org/10.1137/S0036142901384162>.
- [5] F. Bassi and S. Rebay. “A High-Order Accurate Discontinuous Finite Element Method for the Numerical Solution of the Compressible NavierStokes Equations”. In: *Journal of Computational Physics* 131.2 (Mar. 1997), pp. 267–279. ISSN: 0021-9991. DOI: 10.1006/jcph.1996.5572.
- [6] F. Bassi and S. Rebay. “High-Order Accurate Discontinuous Finite Element Solution of the 2D Euler Equations”. In: *Journal of Computational Physics* 138.2 (1997), pp. 251–285. ISSN: 00219991. DOI: 10.1006/jcph.1997.5454.
- [7] F. Bassi et al. “Agglomeration Based Discontinuous Galerkin Discretization of the Euler and Navier-Stokes Equations”. In: *Computers & Fluids*. "High Fidelity Flow Simulations" Onera Scientific Day 61 (May 2012), pp. 77–85. ISSN: 0045-7930. DOI: 10.1016/j.compfluid.2011.11.002.
- [8] F. Bassi et al. “On the Flexibility of Agglomeration Based Physical Space Discontinuous Galerkin Discretizations”. In: *Journal of Computational Physics* 231.1 (Jan. 2012), pp. 45–65. ISSN: 0021-9991. DOI: 10.1016/j.jcp.2011.08.018.
- [9] Francesco Bassi et al. “A High-Order Accurate Discontinuous Finite Element Method for Inviscid and Viscous Turbomachinery Flows”. In: *Proceedings of the 2nd European Conference on Turbomachinery Fluid Dynamics and Thermodynamics*. Antwerpen, Belgium, 1997, pp. 99–109.
- [10] Francesco Bassi et al. “Discontinuous Galerkin Solution of the Reynolds-averaged NavierStokes and kw Turbulence Model Equations”. In: *Computers & Fluids* 34.4-5 (2005), p. 34. DOI: 10.1016/j.compfluid.2003.08.004.
- [11] F. Brezzi et al. “Discontinuous Galerkin Approximations for Elliptic Problems”. In: *Numerical Methods for Partial Differential Equations* 16.4 (2000), pp. 365–378. ISSN: 1098-2426. DOI: 10.1002/1098-2426(200007)16:4<365::AID-NUM2>3.0.CO;2-Y.
- [12] Ismail Celik et al. “Procedure for Estimation and Reporting of Uncertainty Due to Discretization in CFD Applications”. In: *Journal of Fluids Engineering* 130.7 (2008), p. 078001. ISSN: 00982202. DOI: 10.1115/1.2960953.
- [13] Jian Cheng and Tiegang Liu. “A Variational Reconstructed Discontinuous Galerkin Method for the Steady-State Compressible Flows on Unstructured Grids”. In: *Journal of Computational Physics* 380 (Mar. 2019), pp. 65–87. ISSN: 00219991. DOI: 10.1016/j.jcp.2018.11.040.
- [14] Jian Cheng, Tiegang Liu, and Hong Luo. “A Hybrid Reconstructed Discontinuous Galerkin Method for Compressible Flows on Arbitrary Grids”. In: *Computers & Fluids* 139 (Nov. 2016), pp. 68–79. ISSN: 00457930. DOI: 10.1016/j.compfluid.2016.04.001.
- [15] Bernardo Cockburn and Chi-Wang Shu. “The Local Discontinuous Galerkin Method for Time-Dependent Convection-Diffusion Systems”. In: *SIAM Journal on Numerical Analysis* 35.6 (Dec. 1998), pp. 2440–2463. ISSN: 0036-1429, 1095-7170. DOI: 10.1137/S0036142997316712.

- [16] Michael Dumbser. “Arbitrary High Order PNM Schemes on Unstructured Meshes for the Compressible NavierStokes Equations”. In: *Computers & Fluids* 39.1 (Jan. 2010), pp. 60–76. ISSN: 00457930. DOI: 10.1016/j.compfluid.2009.07.003.
- [17] Michael Dumbser and Martin Käser. “Arbitrary High Order Non-Oscillatory Finite Volume Schemes on Unstructured Meshes for Linear Hyperbolic Systems”. In: *Journal of Computational Physics* 221.2 (Feb. 2007), pp. 693–723. ISSN: 00219991. DOI: 10.1016/j.jcp.2006.06.043.
- [18] Michael Dumbser and Olindo Zanotti. “Very High Order PNM Schemes on Unstructured Meshes for the Resistive Relativistic MHD Equations”. In: *Journal of Computational Physics* 228.18 (Oct. 2009), pp. 6991–7006. ISSN: 00219991. DOI: 10.1016/j.jcp.2009.06.009. arXiv: 0903.4832.
- [19] Michael Dumbser et al. “A Unified Framework for the Construction of One-Step Finite Volume and Discontinuous Galerkin Schemes on Unstructured Meshes”. In: *Journal of Computational Physics* 227.18 (Sept. 2008), pp. 8209–8253. ISSN: 00219991. DOI: 10.1016/j.jcp.2008.05.025.
- [20] Cedric Fallet. “Prolongationsoperatoren Für Ein Nichtlineares Mehrgitterverfahren Auf Unstrukturierten Gittern”. Studienarbeit. TU Braunschweig, Nov. 2021.
- [21] Christophe Geuzaine and Jean-François Remacle. “Gmsh: A 3-D Finite Element Mesh Generator with Built-in Pre- and Post-Processing Facilities”. In: *International Journal for Numerical Methods in Engineering* 79.11 (2009), pp. 1309–1331. ISSN: 1097-0207. DOI: 10.1002/nme.2579.
- [22] F. Haider, J.-P. Croisille, and B. Courbet. “Stability Analysis of the Cell Centered Finite-Volume MUSCL Method on Unstructured Grids”. In: *Numerische Mathematik* 113.4 (2009), pp. 555–600. DOI: 10.1007/s00211-009-0242-6.
- [23] Ami Harten. “High Resolution Schemes for Hyperbolic Conservation Laws”. In: *Journal of Computational Physics* 49.3 (Mar. 1983), pp. 357–393. ISSN: 0021-9991. DOI: 10.1016/0021-9991(83)90136-5.
- [24] Ralf Hartmann and Paul Houston. “Symmetric Interior Penalty DG Methods for the Compressible Navier-Stokes Equations I: Method Formulation”. In: *International Journal of numerical Analysis and modeling* 3.1 (2006), p. 20.
- [25] Andreas C. Haselbacher. “A grid-transparent numerical method for compressible viscous flows on mixed unstructured grids”. In: (Nov. 2010). URL: [https://repository.lboro.ac.uk/articles/thesis/A\\_grid-transparent\\_numerical\\_method\\_for\\_compressible\\_viscous\\_flows\\_on\\_mixed\\_unstructured\\_grids/9219554](https://repository.lboro.ac.uk/articles/thesis/A_grid-transparent_numerical_method_for_compressible_viscous_flows_on_mixed_unstructured_grids/9219554).
- [26] Stefan Hickel, Christian P. Egerer, and Johan Larsson. “Subgrid-Scale Modeling for Implicit Large Eddy Simulation of Compressible Flows and Shock-Turbulence Interaction”. In: *Physics of Fluids* 26.10 (Oct. 2014), p. 106101. ISSN: 1070-6631, 1089-7666. DOI: 10.1063/1.4898641.
- [27] Stefan Langer, Axel Schwöppe, and Norbert Kroll. “Investigation and Comparison of Implicit Smoothers Applied in Agglomeration Multigrid”. In: *AIAA Journal* 53.8 (Aug. 2015), pp. 2080–2096. ISSN: 0001-1452, 1533-385X. DOI: 10.2514/1.J053367.
- [28] Randall J. LeVeque. *Finite Volume Methods for Hyperbolic Problems*. Cambridge Texts in Applied Mathematics. Cambridge: Cambridge University Press, 2002. ISBN: 978-0-521-00924-9.
- [29] Lingquan Li et al. “A Discontinuous Galerkin Method Based on Variational Reconstruction for Compressible Flows on Arbitrary Grids”. In: *2018 AIAA Aerospace Sciences Meeting*. Kissimmee, Florida: American Institute of Aeronautics and Astronautics, Jan. 2018. ISBN: 978-1-62410-524-1. DOI: 10.2514/6.2018-0831.
- [30] Xiaodong Liu, Yidong Xia, and Hong Luo. “A Reconstructed Discontinuous Galerkin Method for Compressible Turbulent Flows on 3D Curved Grids”. In: *Computers & Fluids* 160 (Jan. 2018), pp. 26–41. ISSN: 00457930. DOI: 10.1016/j.compfluid.2017.10.014.
- [31] Xiaodong Liu et al. “A Reconstructed Discontinuous Galerkin Method for the Compressible Navier-Stokes Equations on Three-Dimensional Hybrid Grids”. In: *Computers & Fluids* 152 (July 2017), pp. 217–230. ISSN: 00457930. DOI: 10.1016/j.compfluid.2017.04.027.
- [32] Johannes Löwe and Matthias Orlt. “Hp-Adaptation for a Discontinuous Galerkin Method in an Unstructured Flow Solver”. In: *AIAA SCITECH 2022 Forum*. San Diego, CA & Virtual: American Institute of Aeronautics and Astronautics, Jan. 2022. ISBN: 978-1-62410-631-6. DOI: 10.2514/6.2022-1372.

- [33] Hong Luo, Joseph D. Baum, and Rainald Löhner. "A Discontinuous Galerkin Method Based on a Taylor Basis for the Compressible Flows on Arbitrary Grids". In: *Journal of Computational Physics* 227.20 (Oct. 2008), pp. 8875–8893. ISSN: 00219991. DOI: 10.1016/j.jcp.2008.06.035.
- [34] Hong Luo et al. "A Comparative Study of Different Reconstruction Schemes for a Reconstructed Discontinuous Galerkin Method on Arbitrary Grids". In: *20th AIAA Computational Fluid Dynamics Conference*. Honolulu, Hawaii: American Institute of Aeronautics and Astronautics, June 2011. ISBN: 978-1-62410-148-9. DOI: 10.2514/6.2011-3839.
- [35] Hong Luo et al. "A Hermite WENO Reconstruction-Based Discontinuous Galerkin Method for the Euler Equations on Tetrahedral Grids". In: *Journal of Computational Physics* 231.16 (June 2012), pp. 5489–5503. ISSN: 00219991. DOI: 10.1016/j.jcp.2012.05.011.
- [36] Hong Luo et al. "A Parallel, Reconstructed Discontinuous Galerkin Method for the Compressible Flows on Arbitrary Grids". In: *Communications in Computational Physics* 9.2 (Feb. 2011), pp. 363–389. ISSN: 1815-2406, 1991-7120. DOI: 10.4208/cicp.070210.020610a.
- [37] Hong Luo et al. "A Reconstructed Discontinuous Galerkin Method Based on a Hierarchical WENO Reconstruction for Compressible Flows on Tetrahedral Grids". In: *Journal of Computational Physics* 236 (Mar. 2013), pp. 477–492. ISSN: 00219991. DOI: 10.1016/j.jcp.2012.11.026.
- [38] Hong Luo et al. "A Reconstructed Discontinuous Galerkin Method for the Compressible Euler Equations on Arbitrary Grids". In: *19th AIAA Computational Fluid Dynamics*. San Antonio, Texas: American Institute of Aeronautics and Astronautics, June 2009. ISBN: 978-1-62410-137-3. DOI: 10.2514/6.2009-3788.
- [39] Hong Luo et al. "A Reconstructed Discontinuous Galerkin Method for the Compressible NavierStokes Equations on Arbitrary Grids". In: *Journal of Computational Physics* 229.19 (Sept. 2010), pp. 6961–6978. ISSN: 0021-9991. DOI: 10.1016/j.jcp.2010.05.033.
- [40] Dimitri Mavriplis. "Revisiting the Least-Squares Procedure for Gradient Reconstruction on Unstructured Meshes". In: *16th AIAA Computational Fluid Dynamics Conference*. Orlando, Florida: American Institute of Aeronautics and Astronautics, June 2003. ISBN: 978-1-62410-086-4. DOI: 10.2514/6.2003-3986.
- [41] Wim A Mulder and Bram Van Leer. "Experiments with Implicit Upwind Methods for the Euler Equations". In: *Journal of Computational Physics* 59.2 (June 1985), pp. 232–246. ISSN: 00219991. DOI: 10.1016/0021-9991(85)90144-5.
- [42] W. H. Reed and T. R. Hill. "Triangular Mesh Methods for the Neutron Transport Equation". In: Los Alamos Scientific Lab., N.Mex. (USA), Oct. 1973.
- [43] Axel Schwöppe and Boris Diskin. "Accuracy of the Cell-Centered Grid Metric in the DLR TAU-Code". In: *New Results in Numerical and Experimental Fluid Mechanics VIII: Contributions to the 17th STAB/DGLR Symposium Berlin, Germany 2010*. Ed. by Andreas Dillmann et al. Berlin, Heidelberg: Springer Berlin Heidelberg, 2013, pp. 429–437. ISBN: 978-3-642-35680-3. DOI: 10.1007/978-3-642-35680-3\_51.
- [44] Jeffrey Slotnick et al. *CFD Vision 2030 Study: A Path to Revolutionary Computational Aerosciences*. Tech. rep. Washington, D.C.: National Aeronautics and Space Administration, 2014.
- [45] P. SPALART and S. ALLMARAS. "A one-equation turbulence model for aerodynamic flows". In: *30th Aerospace Sciences Meeting and Exhibit*. 1992. DOI: 10.2514/6.1992-439.
- [46] Stanly Steinberg and Patrick J Roache. "Symbolic manipulation and computational fluid dynamics". In: *Journal of Computational Physics* 57.2 (1985), pp. 251–284. ISSN: 0021-9991. DOI: [https://doi.org/10.1016/0021-9991\(85\)90045-2](https://doi.org/10.1016/0021-9991(85)90045-2). URL: <https://www.sciencedirect.com/science/article/pii/0021999185900452>.
- [47] William Sutherland. "LII. The viscosity of gases and molecular force". In: *The London, Edinburgh, and Dublin Philosophical Magazine and Journal of Science* 36.223 (1893), pp. 507–531. DOI: <https://doi.org/10.1080/14786449308620508>.
- [48] Michael Wagner et al. "Spliss: Transparent Integration of Heterogenous HPC Architectures into CFD Solvers and Applications". In: *Methods, Tools and Technologies for Design in Aviation*. Barcelona, Spanien, Nov. 2021.

- [49] Marcel Wallraff and Tobias Leicht. “Higher Order Multigrid Algorithms for a Discontinuous Galerkin RANS Solver”. In: *52nd Aerospace Sciences Meeting*. National Harbor, Maryland: American Institute of Aeronautics and Astronautics, Jan. 2014. ISBN: 978-1-62410-256-1. DOI: 10.2514/6.2014-0936.
- [50] Qian Wang et al. “Compact High Order Finite Volume Method on Unstructured Grids III: Variational Reconstruction”. In: *Journal of Computational Physics* 337 (May 2017), pp. 1–26. ISSN: 00219991. DOI: 10.1016/j.jcp.2017.02.031.
- [51] Yidong Xia et al. “A Set of Parallel, Implicit Methods for a Reconstructed Discontinuous Galerkin Method for Compressible Flows on 3D Hybrid Grids”. In: *Computers & Fluids* 98 (July 2014), pp. 134–151. ISSN: 00457930. DOI: 10.1016/j.compfluid.2014.01.023.
- [52] Zhengqian Xu et al. “A Hybrid Hermite-WENO/Slope Limiter for Reconstructed Discontinuous Galerkin Methods on Unstructured Grids”. In: *Computers & Fluids* 145 (Mar. 2017), pp. 85–98. ISSN: 00457930. DOI: 10.1016/j.compfluid.2016.12.013.
- [53] Fan Zhang, Tiegang Liu, and Moubin Liu. “A Third-Order Weighted Variational Reconstructed Discontinuous Galerkin Method for Solving Incompressible Flows”. In: *Applied Mathematical Modelling* 91 (Mar. 2021), pp. 1037–1060. ISSN: 0307904X. DOI: 10.1016/j.apm.2020.10.011.

# A

## Influence of the weighting on the condition number of reconstruction

The influence of the inverse distance weighting on the stiffness of the reconstruction problems is evaluated on the example of the Multi-element airfoil (section 6.6). For this, the condition number of the reconstruction of each cell is calculated as

$$C = \frac{\lambda_{max}}{\lambda_{min}} \quad (A.1)$$

To identify cells in the boundary layer, the condition number is plotted against the normalised cell value. Cells, which resolve the boundary layer, are comparatively smaller than the cells in the freestream, as can be seen in figure 6.11a. The results can be seen in figure A.1.

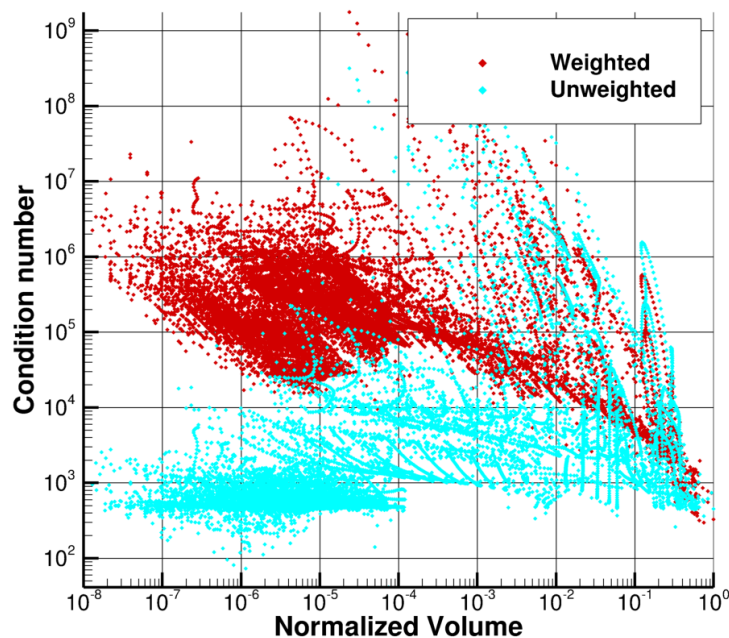


Figure A.1: Condition numbers of the linear reconstruction problems against the normalized volume of the cell.

From the figure it can be seen, that the condition number of the reconstruction problem increases as the cells become smaller only significantly for the weighted least-squares method. Furthermore, as the weighted

least squares method was not observed to be more difficult or expensive to converge, it can be argued that the condition number of the reconstruction does not solely influence the stiffness of the non-linear system.